

# A posteriori error estimates for mixed-dimensional Darcy flow using non-matching grids

Jhabriel Varela<sup>✉\*†‡</sup>      Christian E. Schaerer<sup>✉†</sup>  
Eirik Keilegavlen<sup>✉§</sup>      Inga Berre<sup>✉§</sup>

December 11, 2025

## Abstract

In this article, we extend the *a posteriori* error estimates for hierarchical mixed-dimensional elliptic equations developed in [Varela et al., *J. Numer. Math.*, 48 (2023), pp. 247–280] to the setting of non-matching mixed-dimensional grids. The extension is achieved by introducing transfer grids between the planar subdomain and interface grids, together with stable discrete projection operators for primal (potential) and dual (flux) variables. The proposed non-matching estimators remain fully guaranteed and computable. Numerical experiments, including three-dimensional problems based on community benchmarks for incompressible Darcy flow in fractured porous media, demonstrate reliable performance of the estimators for the non-matching grids and effectivity that is comparable to the estimators for matching grids.

**Keywords:** a posteriori error estimates, mixed-dimensional elliptic equations, non-matching grids, single-phase flow in fractured porous media

**MSC Classification:** 65N15, 65N50, 76S05

---

\*Contact e-mail: [jhabriel@pol.una.py](mailto:jhabriel@pol.una.py)

†Polytechnic School, National University of Asunción, Paraguay

‡Polytechnic University Taiwan-Paraguay, Paraguay

§Center for Modeling of Coupled Subsurface Dynamics, Department of Mathematics, University of Bergen, Norway

# Contents

<b>1</b>	<b>Introduction</b>	<b>3</b>
<b>2</b>	<b>Mixed-dimensional setting and the model problem</b>	<b>4</b>
2.1	Mixed-dimensional decomposition . . . . .	4
2.2	The model problem . . . . .	5
<b>3</b>	<b>Functional framework</b>	<b>7</b>
3.1	Local and global spaces . . . . .	7
3.2	Continuous transfer operators . . . . .	8
3.3	Weak forms . . . . .	9
<b>4</b>	<b>Discrete setting</b>	<b>11</b>
4.1	Grid definitions . . . . .	11
4.2	Discrete projection operators . . . . .	12
4.2.1	Discrete projections for the weak primal problem . . . . .	13
4.2.2	Discrete projections of potentials for the weak dual problem . . . . .	14
4.2.3	Discrete projections of interface fluxes for the weak dual problem . . . . .	15
4.3	Primal and dual approximations . . . . .	17
4.4	Broken energy norms . . . . .	19
<b>5</b>	<b>A posteriori error estimation</b>	<b>19</b>
5.1	A posteriori error estimates . . . . .	20
5.2	Conforming fluxes and potentials . . . . .	21
5.3	Fully computable a posteriori error estimates . . . . .	22
5.4	Error indicators . . . . .	23
5.5	Effectivity indices . . . . .	23
<b>6</b>	<b>Numerical examples</b>	<b>23</b>
6.1	3D/2D verification with a manufactured solution . . . . .	24
6.2	Regular fracture network . . . . .	25
6.3	Production on a fracture network with small features . . . . .	28
<b>7</b>	<b>Conclusion</b>	<b>30</b>

# 1 Introduction

The scalar hierarchical mixed-dimensional (mD) elliptic equation extends the standard Poisson equation by incorporating the coupling between domains of co-dimension one [1]. This framework is particularly well suited for modeling flow processes in fractured porous media [2, 3], where the rock matrix is represented as a 3D host domain, fractures as embedded 2D planar surfaces, fracture intersections as 1D line segments, and their intersections as 0D points. Over the past two decades, this model has been extensively studied, and a variety of techniques have been proposed to solve it; we refer the reader to the review articles [4, 5] and community benchmarks [6, 7] for comprehensive overviews. Notably, the model has been recently validated experimentally [8], further establishing its relevance and applicability.

Given that mD problems naturally span subdomains of different dimensions, it is both geometrically and computationally advantageous to discretize each subdomain with an independent grid, avoiding the constraints of matching grids. Previous works that have considered modeling and discretization of flow in fractured porous media on non-matching grids include [9–13]. In parallel, *a posteriori* error estimates were also developed for problems in mixed dimensions. For instance, [14] in the context of multi-scale mortar methods, [15–19] for Darcy flow in fractured media, and more recently [20] for hierarchical mD elliptic problems in the context of Darcy flow in networks of planar fractures. To our knowledge, however, no existing estimators cover the fully general mD setting—incorporating intersecting and fully embedded subdomains—on non-matching grids.

Motivated by filling this gap, we extend the estimates derived in [20] to the non-matching case. In our context, *non-matching* means that elements in the higher-dimensional grid, the lower-dimensional grid, or both, do not geometrically align with the elements of the coupling interface grid (also known as a mortar grid). However, it is important to remark that all these grids are individually strictly non-overlapping and conforming. Figure 1 illustrates this concept in two dimensions. Non-matching grids enable independent refinement or coarsening of subdomains and interfaces, potentially leading to significant computational savings. For instance, one may refine only the fracture grid in response to large local estimator values, while leaving the surrounding matrix grid unchanged. Such fully disjoint adaptivity avoids the technical complexity of enforcing geometric inter-dimensional conformity.

Extending the validity of the *a posteriori* error estimators from the matching to the general non-matching case is a non-trivial task, as one needs to introduce appropriate mappings of the primal (potentials) and dual (fluxes) variables between subdomains and interfaces while preserving functional conformity in a weak sense. In this work, we overcome this challenge by constructing a *transfer grid* (common refinement grid between subdomains and interfaces), from which potentials and interface fluxes are projected in an energy-consistent manner. This approach allows the estimates of [20] to carry over directly to the non-matching setting. Optimal generation of transfer grids, however, remains a

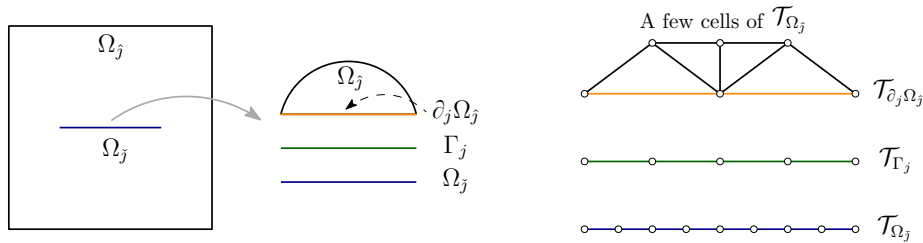


Figure 1: Mixed-dimensional geometric setting. Left: A fracture  $\Omega_j$  fully embedded in the matrix  $\Omega_j$ . A close-up of the upper side of the fracture shows the interface  $\Gamma_j$  coupling  $\Omega_j$  and  $\Omega_j$  through its internal boundary  $\partial_j \Omega_j$ . There exists a similar coupling on the lower side of the fracture, not shown in the figures. Right: A non-matching coupling between  $\mathcal{T}_{\partial_j \Omega_j}$ ,  $\mathcal{T}_{\Gamma_j}$  and  $\mathcal{T}_{\Omega_j}$ . Grids are formally defined in Section 4.1.

challenging task [21–23].

The remainder of the article is organized as follows. In Section 2, we present the mD strong formulations. Section 3 introduces the functional framework, including local and mD spaces and continuous transfer operators. Section 4 covers the discrete setting, formally introducing the grids, discrete projection operators and finite-dimensional approximations. In Section 5, we first develop the abstract and then the fully computable *a posteriori* error estimates. Finally, in Section 6, we present the numerical results and in Section 7 we draw our conclusions.

## 2 Mixed-dimensional setting and the model problem

In this section, we introduce the mD decomposition of the domain together with the strong forms of the model problem.

### 2.1 Mixed-dimensional decomposition

Following the notation introduced in [20], we consider an mD domain  $Y \subset \mathbb{R}^n$ ,  $n \in \{2, 3\}$  decomposed into strictly disjoint and flat subdomains  $\Omega_i$ . Each  $\Omega_i$  has a known dimension  $d_i = d(i)$ , where  $0 \leq d_i \leq n$ . There are  $N_\Omega$  subdomains and we denote by  $I = \{1, 2, \dots, N_\Omega\}$  the index set of all subdomains. As shown in the left panel of Figure 1, interfaces  $\Gamma_j$  establish the connection between two neighboring subdomains that are one dimension apart. Each interface has a known dimension  $d_j = d(j)$ , where  $0 \leq d_j \leq n - 1$ . There are  $N_\Gamma$  interfaces and the index set of interfaces is denoted by  $J = \{1, 2, \dots, N_\Gamma\}$ . For a given interface  $\Gamma_j$ , we use the indices  $\hat{j} \in I$  and  $\check{j} \in I$  to respectively identify higher- and lower-dimensional neighboring subdomains  $\Omega_{\hat{j}}$  and  $\Omega_{\check{j}}$ . The portion of the boundary of

$\Omega_j$  geometrically coinciding with  $\Gamma_j$  is denoted by  $\partial_j\Omega_j$ . We impose the following geometric compatibility conditions for the coupling triplet  $(\partial_j\Omega_j, \Gamma_j, \Omega_j)$ .

**Assumption 1** (Geometric compatibility of the coupling triplet). *Let  $j \in J$  and consider the coupling triplet*

$$(\partial_j\Omega_j, \Gamma_j, \Omega_j),$$

where  $\Gamma_j$  is the interface connecting  $\Omega_j$  and  $\Omega_{\bar{j}}$ .

(i)  $\Omega_i \subset \mathbb{R}^n$  is an open, bounded Lipschitz domain of intrinsic dimension  $d_i \leq n$ . Its boundary  $\partial\Omega_i$  (when  $d_i > 0$ ) is a  $(d_i - 1)$ -dimensional Lipschitz domain.

(ii)  $\Gamma_j$  is a  $d_j$ -dimensional Lipschitz domain with  $d_j = d_{\bar{j}}$ , and there exist bi-Lipschitz homeomorphisms

$$\Psi_j^j : \partial_j\Omega_j \rightarrow \Gamma_j, \quad \Psi_j^{\bar{j}} : \Omega_{\bar{j}} \rightarrow \Gamma_j,$$

with uniformly bounded Lipschitz constants and inverses.

(iii) By means of these maps we identify  $\partial_j\Omega_j$ ,  $\Gamma_j$ , and  $\Omega_{\bar{j}}$  as the same geometric domain up to bi-Lipschitz equivalence.

Given that several interfaces can be associated to a single subdomain, for all  $i \in I$ , we introduce the interface index sets  $\hat{S}_i$  and  $\check{S}_i$  to establish their connections. The set  $\hat{S}_i$  contains the indices of all higher-dimensional neighboring interfaces of the subdomain  $\Omega_i$ . Similarly, the set  $\check{S}_i$  contains the indices of all lower-dimensional neighboring interfaces of the subdomain  $\Omega_i$ . For example, in Figure 2,  $\hat{S}_5 = \{4, 3\}$  and  $\check{S}_5 = \{10\}$ .

Recalling that  $A \sqcup B$  denotes the disjoint union of the sets  $A$  and  $B$ , we define the set of all subdomains by  $\Omega = \sqcup_{i \in I} \Omega_i$  and the set of all interfaces by  $\Gamma = \sqcup_{j \in J} \Gamma_j$ . Thus, a complete disjoint partitioning of the mD domain  $Y$  is given by  $Y = \Omega \sqcup \Gamma$ .

To finalize the geometric description, we define the boundary of  $\Omega$  as  $\partial\Omega = \partial_D\Omega \cup \partial_N\Omega \cup \partial_I\Omega$ , where  $\partial_D\Omega = \cup_{i \in I} \partial_D\Omega_i$ ,  $\partial_N\Omega = \cup_{i \in I} \partial_N\Omega_i$  and  $\partial_I\Omega = \cup_{i \in I} \cup_{j \in \hat{S}_i} \partial_j\Omega_i$  are respectively the Dirichlet, Neumann and internal portions of  $\partial\Omega$ , assumed to be strictly non-overlapping. Since the problem we are interested in is purely elliptic, we require  $\partial_D\Omega \neq \emptyset$ . A full geometric decomposition of an mD domain  $Y \subset \mathbb{R}^2$  is shown schematically in Figure 2.

## 2.2 The model problem

We now present the mD elliptic problem in strong form, in the context of incompressible single phase flow in fractured porous media. For the details, we refer to [2, 3, 24].

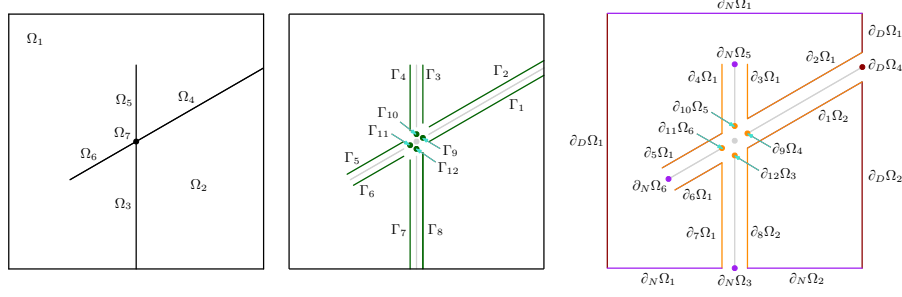


Figure 2: Complete geometric decomposition of an mD domain. Left: Subdomains. Two 2D subdomains ( $\Omega_1$  and  $\Omega_2$ ) hosting four 1D fractures ( $\Omega_3, \Omega_4, \Omega_5, \Omega_6$ ) that intersect at a common 0D point ( $\Omega_7$ ). Center: Interfaces. Twelve interfaces coupling neighboring subdomains of co-dimension one. Right: Internal and external boundary conditions.

**Definition 1** (Strong primal form). *Let  $i \in I$  and  $j \in J$ . Then, find each pressure  $p_i : \Omega_i \rightarrow \mathbb{R}$ , such that*

$$-\nabla_i \cdot (\mathcal{K}_i \nabla_i p_i) + \sum_{j \in \hat{S}_i} \kappa_j (p_j - p_i) = f_i \quad \text{in } \Omega_i, \quad (1a)$$

$$(\mathcal{K}_j \nabla_j p_j) \cdot \mathbf{n}_j = \kappa_j (p_j - p_i) \quad \text{on } \partial_j \Omega_j, \quad (1b)$$

$$(\mathcal{K}_i \nabla_i p_i) \cdot \mathbf{n}_i = 0 \quad \text{on } \partial_N \Omega_i, \quad (1c)$$

$$p_i = g_{D,i} \quad \text{on } \partial_D \Omega_i. \quad (1d)$$

Introducing the subdomain Darcy (tangential) flux  $\mathbf{u}_i = -\mathcal{K}_i \nabla_i p_i$  and the interface (normal) flux  $\lambda_j = -\kappa_j (p_j - p_i)$ , the strong primal form from Definition 1 can be recast into the following dual problem.

**Definition 2** (Strong dual form). *Let  $i \in I$  and  $j \in J$ . Then, find each Darcy flux  $\mathbf{u}_i : \Omega_i \rightarrow \mathbb{R}^{d_i}$ , interface flux  $\lambda_j : \Gamma_j \rightarrow \mathbb{R}$ , and pressure  $p_i : \Omega_i \rightarrow \mathbb{R}$ , such that*

$$\nabla_i \cdot \mathbf{u}_i - \sum_{j \in \hat{S}_i} \lambda_j = f_i \quad \text{in } \Omega_i, \quad (2a)$$

$$\mathbf{u}_i = -\mathcal{K}_i \nabla_i p_i \quad \text{in } \Omega_i, \quad (2b)$$

$$\lambda_j = -\kappa_j (p_j - p_i) \quad \text{on } \Gamma_j, \quad (2c)$$

$$\mathbf{u}_j \cdot \mathbf{n}_j = \lambda_j \quad \text{on } \partial_j \Omega_j, \quad (2d)$$

$$\mathbf{u}_i \cdot \mathbf{n}_i = 0 \quad \text{on } \partial_N \Omega_i, \quad (2e)$$

$$p_i = g_{D,i} \quad \text{on } \partial_D \Omega_i. \quad (2f)$$

In Definitions 1 and 2,  $\nabla_i$  is the  $d_i$ -dimensional *nabla* operator,  $\mathbf{n}_i$  the outward-pointing normal vector on a given Neumann boundary  $\partial_N\Omega_i$  or internal boundary  $\partial_I\Omega_i$ ,  $f_i : \Omega_i \rightarrow \mathbb{R}$  is a source term, and  $g_{D,i} : \partial_D\Omega_i \rightarrow \mathbb{R}$  is the Dirichlet boundary data. Finally,  $\mathcal{K}_i : \Omega_i \rightarrow \mathbb{R}^{d_i \times d_i}$  is the effective permeability matrix and  $\kappa_j : \Gamma_j \rightarrow \mathbb{R}$  is the effective normal permeability. For the physical interpretation of the model, the reader is referred to [3, 20, 25] and the references therein.

**Remark 1.** *The dual form provides a natural framework for coupling non-matching grids, since the introduction of the interface flux  $\lambda_j$  naturally decouples subdomain and interface contributions while strongly imposing inter-dimensional flux continuity.*

### 3 Functional framework

We now define the functional spaces required to formulate the weak versions of Definitions 1 and 2, respectively. From this point onward, we shall use  $\nabla_i(\cdot)$  and  $\nabla_i \cdot (\cdot)$  to denote the  $d_i$ -dimensional weak gradient and divergence operators, respectively.

#### 3.1 Local and global spaces

Let  $S$  denote an open and bounded domain with boundaries satisfying Assumption 1 when applicable. We use  $L^2(S)$  to denote the space of square-integrable functions on  $S$ , equipped with inner product  $(\cdot, \cdot)_S \equiv (\cdot, \cdot)_{L^2(S)}$  and norm  $\|\cdot\|_S \equiv \|\cdot\|_{L^2(S)}$ . We also introduce the space of square-integrable vector-valued functions on  $S$ , that is  $\mathbf{L}^2(S) = [L^2(S)]^{d(S)}$ , with  $d(S)$  denoting the intrinsic dimension of  $S$ . For the sake of compactness we also use  $(\cdot, \cdot)_S \equiv (\cdot, \cdot)_{\mathbf{L}^2(S)}$  and  $\|\cdot\|_S \equiv \|\cdot\|_{\mathbf{L}^2(S)}$  in the vector case.

The standard energy space is defined as  $H^1(\Omega_i) = \{q_i \in L^2(\Omega_i) : \nabla_i q_i \in \mathbf{L}^2(\Omega_i)\}$  while  $H_0^1(\Omega_i) = \{q_i \in H^1(\Omega_i) : q_i|_{\partial_D\Omega_i} = 0\}$  denotes the subspace of  $H^1(\Omega_i)$  of functions with vanishing traces on Dirichlet boundaries. Additionally, we let  $g_i \in H^1(\Omega_i)$  represent any function whose restriction on  $\partial_D\Omega_i$  matches the boundary data, i.e.,  $g_i|_{\partial_D\Omega_i} = g_{D,i}$ . Here,  $(\cdot)|_{\partial_D\Omega_i} : H^1(\Omega_i) \rightarrow H^{1/2}(\partial_D\Omega_i)$  is the trace operator with  $H^{1/2}(\partial_D\Omega_i)$  denoting the fractional Sobolev space on the Dirichlet boundary. Although implicit, it is important to mention that the traces on the internal boundaries also belong to the space  $H^{1/2}(\partial_I\Omega_i)$ .

We now turn our focus to the flux spaces. We define the space  $\mathbf{H}(\text{div}, \Omega_i) = \{\mathbf{v}_i \in \mathbf{L}^2(\Omega_i) : \nabla_i \cdot \mathbf{v}_i \in L^2(\Omega_i)\}$  alongside the subspace  $\mathbf{V}_i = \{\mathbf{v}_i \in \mathbf{H}(\text{div}, \Omega_i) : (\mathbf{v}_i \cdot \mathbf{n}_i)|_{\partial_N\Omega_i} = 0\}$ , which enforces vanishing traces on Neumann boundaries. Similarly, the space  $\mathbf{V}_{0,i} = \{\mathbf{v}_i \in \mathbf{V}_i : (\mathbf{v}_i \cdot \mathbf{n}_i)|_{\partial_I\Omega_i} = 0\}$  consists of functions with vanishing traces on both Neumann and internal boundaries. To handle internal boundaries, following [24], we introduce the linear extension operator

$\mathcal{R}_j : L^2(\Gamma_j) \rightarrow \mathbf{V}_j$ , satisfying for any  $\nu_j \in L^2(\Gamma_j)$ :

$$(\mathcal{R}_j \nu_j)|_{\partial_j \Omega_j} \cdot \mathbf{n}_j = \begin{cases} \nu_j & \text{on } \partial_j \Omega_j, \\ 0 & \text{on } \partial \Omega_j \setminus \partial_j \Omega_j. \end{cases} \quad (3)$$

An explicit form for  $\mathcal{R}_j$  can be obtained by solving an auxiliary elliptic problem [24]. We shall revisit this operator at the end of Section 3.2. The space  $\mathbf{V}_{0,i}$ , together with the linear extension operator  $\mathcal{R}_j$ , allow us to represent, in a weak sense, subdomain fluxes  $\mathbf{v}_i \in \mathbf{V}_i$  with  $(\mathbf{v}_i \cdot \mathbf{n}_i)|_{\partial_j \Omega_j} = \nu_j$  for all  $j \in \check{S}_i$ , as  $\mathbf{v}_i = \mathbf{v}_{0,i} + \sum_{j \in \check{S}_i} \mathcal{R}_j \nu_j$ , with  $\mathbf{v}_{0,i} \in \mathbf{V}_i$  and  $\nu_j \in L^2(\Gamma_j)$ . The above decomposition suggests the following local space for subdomain fluxes

$$\mathbf{X}_i := \mathbf{V}_{0,i} \times \prod_{j \in \check{S}_i} \mathcal{R}_j L^2(\Gamma_j). \quad (4)$$

**Remark 2** ( $\mathbf{X}_i$  vs.  $\mathbf{V}_i$ ). *The space  $\mathbf{X}_i$  has higher regularity compared to  $\mathbf{V}_i$ , as this latter does not contain  $L^2$  traces on internal boundaries. This enhanced regularity on internal boundaries allows the construction of pure  $L^2$ -type projections on coupling triplets in the case of weak dual approximations.*

Global spaces are now immediate by taking the Cartesian product of local spaces,

$$L^2(\Omega) := \prod_{i \in I} L^2(\Omega_i), \quad L^2(\Gamma) := \prod_{j \in J} L^2(\Gamma_j). \quad (5)$$

Analogous definitions hold for  $\mathbf{L}^2(\Omega)$ ,  $H^1(\Omega)$ ,  $H_0^1(\Omega)$ ,  $H^{1/2}(\partial_D \Omega)$ ,  $\mathbf{V}$ ,  $\mathbf{V}_0$ , and  $\mathbf{X}$ . We will later use these spaces to represent weak solutions to the model problem in the mD partition  $\Omega \sqcup \Gamma$ .

### 3.2 Continuous transfer operators

Let  $j \in J$  and consider the coupling triplet  $(\partial_j \Omega_j, \Gamma_j, \Omega_j)$ . Recall that by Assumption 1, the three sets represent the same geometric domain.

**Definition 3** (Continuous transfer operators). *We define bounded linear transfers acting as canonical identifications or embeddings:*

(i) *Transfers between  $\partial_j \Omega_j$  and  $\Gamma_j$ . Define*

$$\mathcal{P}_j^j : H^{1/2}(\partial_j \Omega_j) \rightarrow H^{1/2}(\Gamma_j), \quad \mathcal{D}_j^j : L^2(\partial_j \Omega_j) \rightarrow L^2(\Gamma_j), \quad \mathcal{D}_j^j : L^2(\Gamma_j) \rightarrow L^2(\partial_j \Omega_j),$$

*where  $\mathcal{P}_j^j$  is an  $H^{1/2}$ -identification and  $\mathcal{D}_j^j$  and  $\mathcal{D}_j^j$  are  $L^2$ -identifications.*

(ii) *Transfers between  $\Omega_j$  and  $\Gamma_j$ . Define*

$$\mathcal{P}_j^j : H^1(\Omega_j) \rightarrow H^{1/2}(\Gamma_j), \quad \mathcal{D}_j^j : L^2(\Omega_j) \rightarrow L^2(\Gamma_j), \quad \mathcal{D}_j^j : L^2(\Gamma_j) \rightarrow L^2(\Omega_j),$$

*where  $\mathcal{P}_j^j$  is the standard embedding  $H^1(\Omega_j) \hookrightarrow H^{1/2}(\Gamma_j)$  on the same domain and  $\mathcal{D}_j^j$  and  $\mathcal{D}_j^j$  are  $L^2$ -identifications.*

**Lemma 1** (Basic properties of transfer operators). *For all admissible arguments:*

(i)  $L^2$  norm preservation under identification:

$$\|\mathcal{D}_j^j w\|_{\Gamma_j} = \|w\|_{\partial_j \Omega_j}, \quad \|\mathcal{D}_j^j \nu\|_{\partial_j \Omega_j} = \|\nu\|_{\Gamma_j}, \quad \|\mathcal{D}_j^j w\|_{\Gamma_j} = \|w\|_{\Omega_j}, \quad \|\mathcal{D}_j^j \nu\|_{\Omega_j} = \|\nu\|_{\Gamma_j}.$$

(ii)  $H^{1/2}$  norm preservation under identification:

$$\|\mathcal{P}_j^j q\|_{H^{1/2}(\Gamma_j)} = \|q\|_{H^{1/2}(\partial_j \Omega_j)}.$$

(iii) Sobolev embedding on the same domain:

$$\|\mathcal{P}_j^j q\|_{H^{1/2}(\Gamma_j)} \leq C_{\text{emb}} \|q\|_{H^1(\Omega_j)}.$$

Here,  $\|\cdot\|_{H^1(S)}$  and  $\|\cdot\|_{H^{1/2}(S)}$  are the usual Sobolev norms on the domain  $S$  and  $C_{\text{emb}}$  is the embedding constant, cf. [26].

**Remark 3** (Continuous transfers vs. discrete projections). *The operators  $\mathcal{P}$  and  $\mathcal{D}$  above act as canonical identifications on the common geometry (with norms associated to the target space). They are introduced only to keep notation aligned with the discrete non-matching case, where genuine projections  $\tilde{\mathcal{P}}$  and  $\tilde{\mathcal{D}}$  are required.*

With the interface to internal-boundary  $L^2$ -transfer  $\mathcal{D}_j^j(\cdot)$  defined, the subdomain extension can be written as the following composition:

$$\mathcal{R}_j = \mathcal{R}_j^* \circ \mathcal{D}_j^j : L^2(\Gamma_j) \rightarrow L^2(\partial_j \Omega_j) \rightarrow \mathbf{V}_j, \quad (6)$$

where  $\mathcal{R}_j^*$  is any bounded lifting from the internal boundary into  $\mathbf{V}_j$  (cf. [24]).

### 3.3 Weak forms

Before stating the weak primal and dual forms of Definitions 1 and 2, we make the data regularity explicit in the following assumption. Here and in the following, we shall use the notation  $[\cdot]$  to denote an ordered collection of subdomain and/or interface variables, depending on context.

**Assumption 2** (Data regularity).

(i)  $f = [f_i] \in L^2(\Omega)$ .

(ii)  $g_D = [g_{D,i}] \in H^{1/2}(\partial\Omega)$ .

(iii) For all  $i \in I$ ,  $\mathcal{K}_i$  is SPD and satisfies the usual ellipticity condition

$$c_i^2 |\boldsymbol{\xi}|^2 \leq \mathcal{K}_i \boldsymbol{\xi} \cdot \boldsymbol{\xi} \leq C_i^2 |\boldsymbol{\xi}|^2, \quad \forall \boldsymbol{\xi} \in \mathbb{R}^{d_i}.$$

(iv) For all  $j \in J$ ,  $\kappa_j$  is non-degenerate with bounds

$$0 < \underline{\kappa}_j \leq \kappa_j \leq \bar{\kappa}_j < \infty.$$

**Definition 4** (Weak primal form). Let  $p = [p_i]$  and  $g = [g_i] \in H^1(\Omega)$ . Then, given  $f = [f_i] \in L^2(\Omega)$ , find  $p \in H_0^1(\Omega) + g$  such that

$$\begin{aligned} & \sum_{i \in I} (\mathcal{K}_i \nabla_i p_i, \nabla_i q_i)_{\Omega_i} + \sum_{j \in J} \left( \kappa_j (\mathcal{P}_j^j p_j - \mathcal{P}_j^j p_j|_{\partial_j \Omega_j}), \mathcal{P}_j^j q_j - \mathcal{P}_j^j q_j|_{\partial_j \Omega_j} \right)_{\Gamma_j} \\ & = \sum_{i \in I} (f_i, q_i)_{\Omega_i} \quad \forall q = [q_i] \in H_0^1(\Omega). \end{aligned} \quad (7)$$

**Remark 4** (Well-posedness of the primal form). The bilinear form associated with the primal weak form is symmetric and, provided Assumption 2 holds, coercive on  $H_0^1(\Omega)$ . Consequently, the problem is well-posed and equivalent to finding the unique minimizer  $p \in H_0^1(\Omega) + g$  of the energy functional:

$$\mathcal{J}(q) = \frac{1}{2} \sum_{i \in I} \left\| \mathcal{K}_i^{1/2} \nabla_i q_i \right\|_{\Omega_i}^2 + \frac{1}{2} \sum_{j \in J} \left\| \kappa_j^{1/2} (\mathcal{P}_j^j q_j - \mathcal{P}_j^j q_j|_{\partial_j \Omega_j}) \right\|_{\Gamma_j}^2 - \sum_{i \in I} (f_i, q_i)_{\Omega_i}.$$

**Definition 5** (Dual weak form). Let  $\mathbf{u} = [\mathbf{u}_{0,i}, \lambda_j]$  and  $p = [p_i]$ . Then, given  $f = [f_i] \in L^2(\Omega)$  and  $g_D = [g_{D,i}] \in H^{1/2}(\partial_D \Omega)$ , find  $\mathbf{u} \in \mathbf{X}$  and  $p \in L^2(\Omega)$  such that

$$\begin{aligned} & \sum_{i \in I} \left( \mathcal{K}_i^{-1} \left( \mathbf{u}_{0,i} + \sum_{j \in \tilde{S}_i} \mathcal{R}_j^* \circ \mathcal{D}_j^j \lambda_j \right), \mathbf{v}_{0,i} + \sum_{j \in \tilde{S}_i} \mathcal{R}_j^* \circ \mathcal{D}_j^j \nu_j \right)_{\Omega_i} \\ & - \sum_{i \in I} \left( p_i, \nabla_i \cdot \left( \mathbf{v}_{0,i} + \sum_{j \in \tilde{S}_i} \mathcal{R}_j^* \circ \mathcal{D}_j^j \nu_j \right) + \sum_{j \in \tilde{S}_i} \mathcal{D}_j^j \nu_j \right)_{\Omega_i} + \sum_{j \in J} (\kappa_j^{-1} \lambda_j, \nu_j)_{\Gamma_j} \\ & = - \sum_{i \in I} (g_{D,i}, (\mathbf{v}_{0,i} \cdot \mathbf{n}_i)|_{\partial_D \Omega_i})_{\partial_D \Omega_i} \quad \forall \mathbf{v} = [\mathbf{v}_{0,i}, \nu_j] \in \mathbf{X}. \end{aligned} \quad (8a)$$

$$\begin{aligned} & \sum_{i \in I} \left( \nabla_i \cdot \left( \mathbf{u}_{0,i} + \sum_{j \in \tilde{S}_i} \mathcal{R}_j^* \circ \mathcal{D}_j^j \lambda_j \right), q_i \right)_{\Omega_i} - \sum_{i \in I} \left( \sum_{j \in \tilde{S}_i} \mathcal{D}_j^j \lambda_j, q_i \right)_{\Omega_i} \\ & = \sum_{i \in I} (f_i, q_i)_{\Omega_i} \quad \forall q = [q_i] \in L^2(\Omega). \end{aligned} \quad (8b)$$

**Remark 5** (Well-posedness of the dual form). The dual form exhibits a saddle-point structure. Well-posedness can be proven using inf-sup arguments [24], provided the data satisfies Assumption 2.

Later, we shall employ the energy norm to measure the *a posteriori* error estimates. For an mD potential function  $q = [q_i] \in H_0^1(\Omega)$  we define

$$\|q\|^2 = \sum_{i \in I} \left\| \mathcal{K}_i^{1/2} \nabla_i q_i \right\|_{\Omega_i}^2 + \sum_{j \in J} \left\| \kappa_j^{1/2} (\mathcal{P}_j^j q_j - \mathcal{P}_j^j q_j|_{\partial_j \Omega_j}) \right\|_{\Gamma_j}^2. \quad (9)$$

For an mD flux function  $\mathbf{v} = [\mathbf{v}_{0,i}, \nu_j] \in \mathbf{L}^2(\Omega) \times L^2(\Gamma)$ , we define the energy norm

$$\|\mathbf{v}\|_*^2 = \sum_{i \in I} \left\| \kappa_i^{-1/2} \left( \mathbf{v}_{0,i} + \sum_{j \in \tilde{S}_i} \mathcal{R}_j^* \circ \mathcal{D}_j^j \nu_j \right) \right\|_{\Omega_i}^2 + \sum_{j \in J} \left\| \kappa_j^{-1/2} \nu_j \right\|_{\Gamma_j}^2. \quad (10)$$

We will use both norms to present the guaranteed upper bounds on the primal (the mD potential) and dual (the mD flux) variables.

## 4 Discrete setting

In this section, we formally introduce the grids and define the discrete projection operators. From there, we write the approximated primal and dual problems and then establish the connection between continuous and broken norms.

### 4.1 Grid definitions

For all  $i \in I$ , we denote by  $\mathcal{T}_{\Omega_i}$  a simplicial and strictly non-overlapping partition of  $\Omega_i$ , such that

$$\overline{\Omega_i} = \bigcup_{K \in \mathcal{T}_{\Omega_i}} K, \quad \dim(K) \in \{0, 1, 2, 3\}.$$

Similarly, for all  $j \in J$ , we denote by  $\mathcal{T}_{\Gamma_j}$  a simplicial and strictly non-overlapping partition of  $\Gamma_j$ , such that

$$\overline{\Gamma_j} = \bigcup_{K \in \mathcal{T}_{\Gamma_j}} K, \quad \dim(K) \in \{0, 1, 2\}.$$

Let  $e$  denote a face from the set of faces  $\mathcal{E}_K$  of an element  $K \in \mathcal{T}_{\Omega_i}$ . For a fixed  $j \in J$ , we define the internal boundary grid as

$$\mathcal{T}_{\partial_j \Omega_j} := \left( \bigcup_{K \in \mathcal{T}_{\Omega_j}} \bigcup_{e \in \mathcal{E}_K} e \right) \cap \partial_j \Omega_j, \quad \overline{\partial_j \Omega_j} = \bigcup_{K \in \mathcal{T}_{\partial_j \Omega_j}} K, \quad \dim(K) \in \{0, 1, 2\}.$$

As illustrated in the right panel of Figure 1, we allow the grid triplet  $(\mathcal{T}_{\partial_j \Omega_j}, \mathcal{T}_{\Gamma_j}, \mathcal{T}_{\Omega_i})$  to be non-matching. When necessary, we shall use  $K_X$  to denote an element of any admissible grid  $\mathcal{T}_X$ .

To ensure the stability of the discrete projection operators that will be constructed next, we require all partitions of subdomains and interfaces to be shape-regular.

**Assumption 3** (Shape-regularity of mixed-dimensional meshes). *There exists  $\vartheta > 0$  such that every simplex  $K$  in each mesh  $\mathcal{T}_{\Omega_i}$ ,  $\mathcal{T}_{\Gamma_j}$ ,  $\mathcal{T}_{\partial_j \Omega_j}$  satisfies  $h_K / \rho_K \leq \vartheta$ , where  $h_K$  is the diameter and  $\rho_K$  the inradius of  $K$ . All meshes are conforming on their respective domains.*

Before defining the discrete projection operators, we need to introduce the *transfer grid* between subdomain and interface grids. This grid facilitates the coupling of non-matching grids by resolving the geometric mismatch between them. We focus our exposition on the 3D case (2D interface grid) as the 2D case (1D interface grid) involves fewer geometric complexities.

**Definition 6** (Transfer grid). *Let  $j \in J$  and  $(\mathcal{T}_{\partial_j \Omega_j}, \mathcal{T}_{\Gamma_j}, \mathcal{T}_{\Omega_j})$  be a coupling grid triplet. We construct the transfer grid  $\mathcal{T}_{\Gamma_j, X}$  with  $X \in \{\partial_j \Omega_j, \Omega_j\}$  via a two-step process. First, identify the set of nodes  $\mathcal{V}_{\Gamma_j, X} = \mathcal{V}_{\Gamma_j} \cup \mathcal{V}_X$  of the transfer grid, with  $\mathcal{V}_{\Gamma_j}$  and  $\mathcal{V}_X$  denoting the set of nodes of  $\mathcal{T}_{\Gamma_j}$  and  $\mathcal{T}_X$ , respectively. Next, for each pair of elements  $K_{\Gamma_j}$  and  $K_X$ , define*

$$S_{\Gamma_j, X} := K_{\Gamma_j} \cap K_X. \quad (11)$$

The above intersections result in one of the following three cases:

- (i) *Polygonal domain. If  $S_{\Gamma_j, X}$  is a triangle, then  $K_{\Gamma_j, X} := S_{\Gamma_j, X}$ , and we include it directly in  $\mathcal{T}_{\Gamma_j, X}$ . Otherwise,  $S_{\Gamma_j, X}$  is a non-simplex macro-element and it must be triangulated into simplicial elements.*
- (ii) *Line segment. If  $S_{\Gamma_j, X}$  is a line-segment, it represents a shared boundary between two elements and does not contribute as an element to  $\mathcal{T}_{\Gamma_j, X}$ .*
- (iii) *Empty intersection. If  $S_{\Gamma_j, X}$  is void, we ignore it.*

Figure 3 shows examples of 1D and 2D transfer grids. To finalize this section, we summarize the geometric properties of the transfer grid.

**Remark 6** (Properties of the transfer grid). *The transfer grid  $\mathcal{T}_{\Gamma_j, X}$  has the properties of node inclusion, refinement, dimensionality, and partitioning:*

- (i)  $\mathcal{V}_{\Gamma_j} \subseteq \mathcal{V}_{\Gamma_j, X}$ ,  $\mathcal{V}_X \subseteq \mathcal{V}_{\Gamma_j, X}$ .
- (ii)  $|\mathcal{T}_{\Gamma_j}| \leq |\mathcal{T}_{\Gamma_j, X}|$ ,  $|\mathcal{T}_X| \leq |\mathcal{T}_{\Gamma_j, X}|$ .
- (iii) For all  $K \in \mathcal{T}_{\Gamma_j, X}$ ,  $\dim(K) = d_j$ .
- (iv) By Assumption 1,  $\overline{\Gamma_j} = \bigcup_{K \in \mathcal{T}_{\Gamma_j, X}} K$ ,  $\overline{X} = \bigcup_{K \in \mathcal{T}_{\Gamma_j, X}} K$ .

## 4.2 Discrete projection operators

To define the discrete projection operators, we shall make extensive use of the broken spaces of polynomials. For  $k \geq 0$  and any mesh  $\mathcal{T}_X$  on a geometric set  $X$ , we define

$$\mathbb{P}_k(\mathcal{T}_X) := \{q_h \in L^2(X) : q_h|_K \in \mathbb{P}_k(K) \ \forall K \in \mathcal{T}_X\}. \quad (12)$$

Functions in  $\mathbb{P}_k(\mathcal{T}_X)$  are generally discontinuous across inter-element boundaries and are not required to satisfy any external boundary condition.

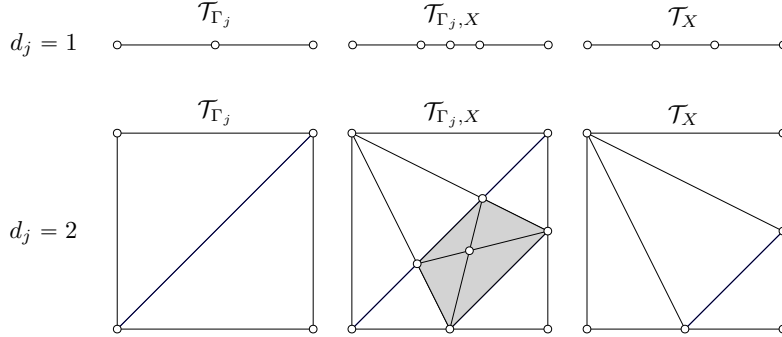


Figure 3: Transfer grids  $\mathcal{T}_{\Gamma_j, X}$  coupling interface grids  $\mathcal{T}_{\Gamma_j}$  with  $\mathcal{T}_X$ ,  $X \in \{\partial_j \Omega_j, \Omega_j\}$ . Top: 1D coupling. Bottom: 2D coupling. The shaded quadrilateral corresponds to a macro-element  $S_{\Gamma_j, X}$  that was further refined into four simplices using its barycenter coordinate.

#### 4.2.1 Discrete projections for the weak primal problem

The projection of potentials for the weak primal problem on non-matching grids is carried out in two stages. First, potentials defined on the source grids (the internal boundary grids and lower-dimensional subdomain grids) are prolonged onto the corresponding transfer grids. Second, the potentials are projected onto the target interface grid using the Scott-Zhang quasi-interpolant.

To be precise, let  $j \in J$  be fixed and let  $(\partial_j \Omega_j, \Gamma_j, \Omega_j)$  be a coupling triplet. For  $k \geq 1$ , we define the prolongation operators

$$\tilde{\mathcal{P}}_j^{j, \hat{j}} : \mathbb{P}_k(\mathcal{T}_{\partial_j \Omega_j}) \cap H^{1/2}(\partial_j \Omega_j) \rightarrow \mathbb{P}_k(\mathcal{T}_{\Gamma_j, \partial_j \Omega_j}) \cap H^{1/2}(\partial_j \Omega_j), \quad (13a)$$

$$\tilde{\mathcal{P}}_j^{j, \check{j}} : \mathbb{P}_k(\mathcal{T}_{\Omega_j}) \cap (H^1(\Omega_j) + g_j) \rightarrow \mathbb{P}_k(\mathcal{T}_{\Gamma_j, \Omega_j}) \cap (H^1(\Omega_j) + g_j), \quad (13b)$$

where the transfer grids  $\mathcal{T}_{\Gamma_j, \partial_j \Omega_j}$  and  $\mathcal{T}_{\Gamma_j, \Omega_j}$  are defined as in Definition 6. Since  $\mathcal{T}_{\Gamma_j, X}$  is a subdivision of  $\mathcal{T}_X$ , for any potential  $q_h \in \mathbb{P}_k(\mathcal{T}_{\partial_j \Omega_j}) \cap H^{1/2}(\partial_j \Omega_j)$ , (13a) satisfies

$$(\tilde{\mathcal{P}}_j^{j, \hat{j}} q_h)|_{K_{\Gamma_j, \partial_j \Omega_j}} = q_h|_{K_{\partial_j \Omega_j}}, \quad \forall K_{\Gamma_j, \partial_j \Omega_j} \in S_{\Gamma_j, \partial_j \Omega_j}, \quad (14)$$

for each transfer macro-element  $S_{\Gamma_j, \partial_j \Omega_j}$  and for each  $K_{\partial_j \Omega_j} \subseteq S_{\Gamma_j, \partial_j \Omega_j}$ . The operator  $\tilde{\mathcal{P}}_j^{j, \check{j}}$  from (13b) satisfies an analogous property for potentials defined on  $\mathcal{T}_{\Omega_j}$ .

Once functions have been prolonged to the transfer grids, we project them onto the target interface grid:

$$\tilde{\mathcal{P}}_{j, \hat{j}}^j : \mathbb{P}_k(\mathcal{T}_{\Gamma_j, \partial_j \Omega_j}) \cap H^{1/2}(\partial_j \Omega_j) \rightarrow \mathbb{P}_k(\mathcal{T}_{\Gamma_j}) \cap H^{1/2}(\Gamma_j), \quad (15a)$$

$$\tilde{\mathcal{P}}_{j, \check{j}}^j : \mathbb{P}_k(\mathcal{T}_{\Gamma_j, \Omega_j}) \cap (H^1(\Omega_j) + g_j) \rightarrow \mathbb{P}_k(\mathcal{T}_{\Gamma_j}) \cap H^{1/2}(\Gamma_j). \quad (15b)$$

Here,  $\tilde{\mathcal{P}}_{j, \hat{j}}^j$  and  $\tilde{\mathcal{P}}_{j, \check{j}}^j$  denote Scott-Zhang quasi-interpolators constructed on  $\mathcal{T}_{\Gamma_j}$ , see [27] for the details.

**Definition 7** (Discrete projections for the primal problem). *Let  $j \in J$  and consider the coupling triplet  $(\partial_j \Omega_j, \Gamma_j, \Omega_j)$ . For a fixed degree  $k \geq 1$ , the discrete projections for the weak primal problem are given by the following compositions*

$$\tilde{\mathcal{P}}_j^j := \tilde{\mathcal{P}}_{j,\hat{j}}^j \circ \tilde{\mathcal{P}}_{\hat{j}}^{j,\hat{j}}, \quad \tilde{\mathcal{P}}_j^j := \tilde{\mathcal{P}}_{j,\hat{j}}^j \circ \tilde{\mathcal{P}}_{\hat{j}}^{j,\hat{j}}. \quad (16)$$

The following lemma establishes a key stability result for the projection operators.

**Lemma 2** (Stability of discrete projection operators for the weak primal problem). *Let  $j \in J$  and  $k \geq 1$ . Then, the operators  $\tilde{\mathcal{P}}_j^j$  and  $\tilde{\mathcal{P}}_{\hat{j}}^{j,\hat{j}}$  in (16) are linear and bounded:*

$$\|\tilde{\mathcal{P}}_j^j q_h\|_{H^{1/2}(\Gamma_j)} \leq C_1 \|q_h\|_{H^{1/2}(\partial_j \Omega_j)}, \quad \|\tilde{\mathcal{P}}_{\hat{j}}^{j,\hat{j}} \phi_h\|_{H^{1/2}(\Gamma_j)} \leq C_2 \|\phi_h\|_{H^1(\Omega_j)},$$

with constants  $C_1$  and  $C_2$  depending only on the shape-regularities of the target and source grids and on the polynomial degree  $k$ .

*Proof.* The prolongation operators are isometric identifications on an equal or more refined partition of the same domain; thus norm preserving in  $H^s$ ,  $s \in [0, 1]$  (see e.g., [28, 29]). The Scott-Zhang quasi-interpolant on the target interface grid is linear and  $H^s$ -stable for  $s \in [0, 1]$  [27]. Setting  $s = 1/2$  yields the first bound. For the second bound, use the Scott-Zhang stability with  $s = 1$  and then the continuous embedding  $H^1(\Gamma_j) \hookrightarrow H^{1/2}(\Gamma_j)$ , cf. Section 4.8 of [30].  $\square$

We emphasize that the stability results in Lemma 2 (and for the ones from the next section) are independent from the transfer grids, as they act purely as data identifiers (stability constants equal to one). This result is numerically verified in Section 6.1.

#### 4.2.2 Discrete projections of potentials for the weak dual problem

We now construct  $L^2$ -type discrete projections of potentials for the weak dual problem. These projections map traces from the internal boundary and lower-dimensional grids onto the interface grid. As in the weak primal case, we proceed in two stages: (i) elementwise prolongation to a transfer grid that resolves the geometric mismatch, and (ii) an  $L^2$ -projection onto the target interface grid.

Fix  $j \in J$  and consider the coupling triplet  $(\partial_j \Omega_j, \Gamma_j, \Omega_j)$  with transfer grids  $\mathcal{T}_{\Gamma_j, \partial_j \Omega_j}$  and  $\mathcal{T}_{\Gamma_j, \Omega_j}$  from Definition 6. For  $k \geq 0$ , define the prolongation operators

$$\tilde{\mathcal{D}}_j^{j,\hat{j}} : \mathbb{P}_k(\mathcal{T}_{\partial_j \Omega_j}) \longrightarrow \mathbb{P}_k(\mathcal{T}_{\Gamma_j, \partial_j \Omega_j}), \quad (17a)$$

$$\tilde{\mathcal{D}}_j^{j,\hat{j}} : \mathbb{P}_k(\mathcal{T}_{\Omega_j}) \longrightarrow \mathbb{P}_k(\mathcal{T}_{\Gamma_j, \Omega_j}), \quad (17b)$$

such that, for every macro-element  $S_{\Gamma_j, X}$  ( $X \in \{\partial_j \Omega_j, \Omega_j\}$ ) and the unique source element  $K_X$  with  $S_{\Gamma_j, X} \subset K_X$ , we have the exact restriction  $(\cdot)|_{S_{\Gamma_j, X}} = (\cdot)|_{K_X}$ . Thus, functions prolonged to the transfer grid are in general discontinuous across transfer elements.

Let  $\{\phi_i^K\}_{i=1}^{N_k}$  be a basis of  $\mathbb{P}_k(K)$  for each interface element  $K \in \mathcal{T}_{\Gamma_j}$ . The  $L^2$ -projection onto  $\mathbb{P}_k(K)$  is obtained by solving the local system  $M^K \alpha^K = b^K$ , where

$$M_{ij}^K = (\phi_i^K, \phi_j^K)_K, \quad b_i^K = (w_h, \phi_i^K)_K = \sum_{K_{\Gamma_j, X} \subset K} (w_h, \phi_i^K)_{K_{\Gamma_j, X}}, \quad (18)$$

with  $w_h$  denoting the prolonged function produced by (17a)–(17b) and the sum is taken over all transfer elements  $K_{\Gamma_j, X} \in \mathcal{T}_{\Gamma_j, X}$  geometrically contained in  $K \in \mathcal{T}_{\Gamma_j}$ .

**Definition 8** (Discrete projections of potentials for the dual problem). *Let  $j \in J$  and consider the coupling triplet  $(\partial_j \Omega_j, \Gamma_j, \Omega_j)$ . For a fixed degree  $k \geq 0$ , the discrete projections of potentials for the weak dual problem are given by compositions*

$$\tilde{\mathcal{D}}_j^j := \tilde{\mathcal{D}}_{j, \hat{j}}^j \circ \tilde{\mathcal{D}}_{\hat{j}}^{j, \hat{j}}, \quad \tilde{\mathcal{D}}_j^j := \tilde{\mathcal{D}}_{j, \hat{j}}^j \circ \tilde{\mathcal{D}}_{\hat{j}}^{j, \hat{j}}. \quad (19)$$

**Lemma 3** (Stability of discrete projections of potentials for the dual problem). *The operators  $\tilde{\mathcal{D}}_j^j$  and  $\tilde{\mathcal{D}}_{\hat{j}}^{j, \hat{j}}$  are linear,  $L^2(\Gamma_j)$ -stable and satisfy, for all admissible sources,*

$$\|\tilde{\mathcal{D}}_j^j q_h\|_{\Gamma_j} \leq C_3 \|q_h\|_{\partial_j \Omega_j}, \quad \|\tilde{\mathcal{D}}_{\hat{j}}^{j, \hat{j}} \varphi_h\|_{\Gamma_j} \leq C_4 \|\varphi_h\|_{\Omega_j}, \quad (20)$$

where  $C_3$  and  $C_4$  depend only on the shape-regularities of source and target grids and on the polynomial degree  $k$ .

*Proof.* The prolongation step acts as an isometric identification on each transfer sub-element and is therefore  $L^2$ -stable. The projection onto the target interface grid is the standard elementwise  $L^2$ -orthogonal projector, hence locally stable and the best-approximation property holds by orthogonality. Global bounds follow from uniform shape-regularity and the fact that, for each target element  $K \in \mathcal{T}_{\Gamma_j}$ , only finitely many transfer elements  $K_{\Gamma_j, X} \subset K$  contribute to the local projection.  $\square$

**Remark 7** (Discrete projections of potentials for dual approximations of the lowest order). *For the lowest-order case  $k = 0$ , the projection amounts to elementwise averages on  $\mathcal{T}_{\Gamma_j}$ , i.e., a weighted sum with weights proportional to the measures of the overlaps  $K_{\Gamma_j, X} \subset K$ .*

### 4.2.3 Discrete projections of interface fluxes for the weak dual problem

We construct discrete projections for interface fluxes onto the internal boundary  $\mathcal{T}_{\partial_j \Omega_j}$  and the lower-dimensional grid  $\mathcal{T}_{\Omega_j}$ , while preserving the elementwise mass on the target grids. The construction consists of (i) a prolongation to a transfer grid and (ii) an agglomeration on the target grid via a constrained  $L^2$  projection enforcing cell mean.

Fix  $j \in J$  and the coupling triplet  $(\partial_j \Omega_j, \Gamma_j, \Omega_j)$  with transfer grids  $\mathcal{T}_{\Gamma_j, \partial_j \Omega_j}$  and  $\mathcal{T}_{\Gamma_j, \Omega_j}$  from Definition 6. For  $k \geq 0$  and  $\nu_h \in \mathbb{P}_k(\mathcal{T}_{\Gamma_j})$ , define the elementwise prolongations

$$\tilde{\mathcal{D}}_j^{j, \hat{j}} : \mathbb{P}_k(\mathcal{T}_{\Gamma_j}) \rightarrow \mathbb{P}_k(\mathcal{T}_{\Gamma_j, \partial_j \Omega_j}), \quad (21a)$$

$$\tilde{\mathcal{D}}_j^{j, \check{j}} : \mathbb{P}_k(\mathcal{T}_{\Gamma_j}) \rightarrow \mathbb{P}_k(\mathcal{T}_{\Gamma_j, \Omega_j}), \quad (21b)$$

by elementwise value restriction:  $(\cdot)|_{S_{\Gamma_j, X}} = (\cdot)|_{K_{\Gamma_j}}$  for each macro-element  $S_{\Gamma_j, X} \subset K_{\Gamma_j}$  and  $X \in \{\partial_j \Omega_j, \Omega_j\}$ . As in Section 4.2.2, the restricted functions are generally discontinuous across transfer elements. Given the prolonged data  $\nu_h$  on  $\mathcal{T}_{\Gamma_j, X}$  for  $X \in \{\partial_j \Omega_j, \Omega_j\}$ , we perform a constrained  $L^2$  agglomeration on the target cell  $K \in \mathcal{T}_X$ . Let  $\{\phi_i^K\}_{i=1}^{N_k}$  be a basis of  $\mathbb{P}_k(K)$ . Assemble  $M_i^K$  and  $b_i^K$  as in (18) and additionally define the mass constraints

$$c_i^K = (1, \phi_i^K)_K, \quad m^K = \sum_{K_{\Gamma_j, X} \subset K} (\nu_h, 1)_{K_{\Gamma_j, X}}. \quad (22)$$

The coefficients  $\alpha^K$  and the Lagrange multiplier  $\mu^K$  are determined from the local constrained optimization problem

$$\begin{bmatrix} M^K & c^K \\ (c^K)^\top & 0 \end{bmatrix} \begin{bmatrix} \alpha^K \\ \mu^K \end{bmatrix} = \begin{bmatrix} b^K \\ m^K \end{bmatrix}. \quad (23)$$

The unique solvability of this system is guaranteed for any  $k \geq 0$ . The local mass matrix  $M^K$  is SPD and since  $1 \in \mathbb{P}_k(K)$ , the constraint vector  $c^K$  is non-zero. This ensures the satisfaction of the inf-sup condition for the Lagrange multiplier  $\mu^K$ . Consequently, the resulting polynomial on  $K$  is  $(\tilde{\mathcal{D}}_{j, j}^{\hat{j}} \nu_h)|_K = \sum_{i=1}^{N_k} \alpha_i^K \phi_i^K$  and analogously for  $\tilde{\mathcal{D}}_{j, j}^{\check{j}}(\cdot)$  on  $\mathcal{T}_{\Omega_j}$ .

**Definition 9** (Discrete projections of interface fluxes for the dual problem). *Let  $j \in J$  and consider the coupling triplet  $(\partial_j \Omega_j, \Gamma_j, \Omega_j)$ . For a fixed degree  $k \geq 0$ , the discrete projections of interface fluxes for the weak dual problem are given by compositions*

$$\tilde{\mathcal{D}}_j^{\hat{j}} := \tilde{\mathcal{D}}_{j, \hat{j}}^{\hat{j}} \circ \tilde{\mathcal{D}}_j^{j, \hat{j}}, \quad \tilde{\mathcal{D}}_j^{\check{j}} := \tilde{\mathcal{D}}_{j, \check{j}}^{\check{j}} \circ \tilde{\mathcal{D}}_j^{j, \check{j}}. \quad (24)$$

The resulting mapping preserves elementwise mass and inherits stability from the constrained  $L^2$  projection.

**Lemma 4** (Stability of discrete projections of interface fluxes for the dual problem). *The operators  $\tilde{\mathcal{D}}_j^{\hat{j}}$  and  $\tilde{\mathcal{D}}_j^{\check{j}}$  are linear,  $L^2$ -stable, and satisfy*

$$\|\tilde{\mathcal{D}}_j^{\hat{j}} \nu_h\|_{\partial_j \Omega_j} \leq C_5 \|\nu_h\|_{\Gamma_j}, \quad \|\tilde{\mathcal{D}}_j^{\check{j}} \nu_h\|_{\Omega_j} \leq C_6 \|\nu_h\|_{\Gamma_j}, \quad (25)$$

with constants depending only on mesh shape-regularity and the degree  $k$ . Moreover, for each  $K \in \mathcal{T}_{\partial_j \Omega_j}$ , the local polynomial  $(\tilde{\mathcal{D}}_j^{\hat{j}} \nu_h)|_K$  is characterized as the unique solution of the constrained minimization problem

$$(\tilde{\mathcal{D}}_j^{\hat{j}} \nu_h)|_K = \arg \min_{\varphi \in \mathbb{P}_k(K)} \{ \|\varphi - \nu_h\|_K : (\varphi, 1)_K = m^K \}, \quad (26)$$

and an analogous statement holds for  $\tilde{\mathcal{D}}_j^{\check{j}}(\cdot)$  on  $\mathcal{T}_{\Omega_j}$ .

Table 1: Summary of discrete projection operators of potentials and interface fluxes for the primal and dual weak problems on non-matching grids.

Discrete operator	Problem	Projected quantity	Source grid	Target grid
$\tilde{\mathcal{P}}_j^j$	Primal	Potential	$\mathcal{T}_{\partial_j \Omega_j}$	$\mathcal{T}_{\Gamma_j}$
$\tilde{\mathcal{P}}_j^j$	Primal	Potential	$\mathcal{T}_{\Omega_j}$	$\mathcal{T}_{\Gamma_j}$
$\tilde{\mathcal{D}}_j^j$	Dual	Potential	$\mathcal{T}_{\partial_j \Omega_j}$	$\mathcal{T}_{\Gamma_j}$
$\tilde{\mathcal{D}}_j^j$	Dual	Potential	$\mathcal{T}_{\Omega_j}$	$\mathcal{T}_{\Gamma_j}$
$\tilde{\mathcal{D}}_j^j$	Dual	Flux	$\mathcal{T}_{\Gamma_j}$	$\mathcal{T}_{\partial_j \Omega_j}$
$\tilde{\mathcal{D}}_j^j$	Dual	Flux	$\mathcal{T}_{\Omega_j}$	$\mathcal{T}_{\Omega_j}$

The argument follows verbatim from Lemma 3: the prolongation is an  $L^2$ -isometry on each transfer element and the constrained  $L^2$  projection is  $L^2$ -stable on shape-regular meshes. Importantly, the discrete projection operator  $\tilde{\mathcal{D}}_j^j$  is locally mass-conservative, in the sense that for any  $\nu_h \in \mathbb{P}_k(\mathcal{T}_{\Gamma_j})$ , there holds

$$(\tilde{\mathcal{D}}_j^j \nu_h, 1)_K = m^K \quad \text{with} \quad m^K = \sum_{K_{\Gamma_j, x} \subset K} (\nu_h, 1)_{K_{\Gamma_j, x}}. \quad (27)$$

That is, the total interface flux over  $K$  equals the sum of incoming fluxes on all transfer grid elements  $K_{\Gamma_j, \partial_j \Omega_j}$  contained in  $K$ . The same property holds for  $\tilde{\mathcal{D}}_j^j(\cdot)$  on  $\mathcal{T}_{\Omega_j}$ .

**Remark 8** (Discrete projections of interface fluxes for dual approximations of the lowest-order). *In the lowest-order case  $k = 0$ , (23) reduces to the overlap-weighted average on each target element:*

$$(\tilde{\mathcal{D}}_{j,j}^j \nu_h)|_K = \frac{1}{|K|} \sum_{K_{\Gamma_j, \partial_j \Omega_j} \subset K} (\nu_h, 1)_{K_{\Gamma_j, \partial_j \Omega_j}} = \frac{1}{|K|} \sum_{K_{\Gamma_j, \partial_j \Omega_j} \subset K} |K_{\Gamma_j, \partial_j \Omega_j}| \nu_h|_{K_{\Gamma_j, \partial_j \Omega_j}}.$$

*An analogous property holds for projection onto the low-dimensional subdomain grid.*

In Table 1, we summarize the six discrete projection operators introduced in this section.

### 4.3 Primal and dual approximations

With the discrete projections operators formally defined, we can now write the approximated primal weak and dual problems. To this aim, consider first the

mD broken space of polynomials on subdomains of order  $k$  or less:

$$\mathbb{P}_k(\mathcal{T}_\Omega) := \prod_{i \in I} \mathbb{P}_k(\mathcal{T}_{\Omega_i}). \quad (28)$$

**Definition 10** (Approximated weak primal form on non-matching grids). *Let  $k \geq 1$  be fixed and  $p_h = [p_{h,i}]$ ,  $g = [g_i] \in H^1(\Omega)$ . Then, given  $f = [f_i] \in L^2(\Omega)$ , find  $p_h \in \mathbb{P}_k(\mathcal{T}_\Omega) \cap (H_0^1(\Omega) + g)$  such that*

$$\begin{aligned} & \sum_{i \in I} \sum_{K \in \mathcal{T}_{\Omega_i}} (\mathcal{K}_i \nabla_i p_{h,i}, \nabla_i q_{h,i})_K + \sum_{j \in J} \sum_{K \in \mathcal{T}_{\Gamma_j}} \left( \kappa_j (\tilde{\mathcal{P}}_j^j p_{h,j} - \tilde{\mathcal{P}}_j^j p_{h,j}), \tilde{\mathcal{P}}_j^j q_{h,j} - \tilde{\mathcal{P}}_j^j q_{h,j} \right)_K \\ & = \sum_{i \in I} \sum_{K \in \mathcal{T}_{\Omega_i}} (f_i, q_{h,i})_K \quad \forall q_h = [q_{h,i}] \in \mathbb{P}_k(\mathcal{T}_\Omega) \cap H_0^1(\Omega). \end{aligned} \quad (29)$$

Consider now the dual approximated problem. We wish to construct the discrete space for the mD fluxes, i.e., the discrete counterpart of  $\mathbf{X}$ . To this aim, we first consider the local Raviart-Thomas space given by

$$\mathbb{RT}_k(\mathcal{T}_{\Omega_i}) = \{ \mathbf{v}_{h,i} \in \mathbf{H}(\text{div}, \Omega_i) : \mathbf{v}_{h,i}|_K \in \mathbb{RT}_k(K) \forall K \in \mathcal{T}_{\Omega_i} \}. \quad (30)$$

Then, the space  $\mathbf{X}_k$  is given by

$$\mathbf{X}_k = \prod_{i \in I} \left[ (\mathbb{RT}_k(\mathcal{T}_{\Omega_i}) \cap \mathbf{V}_{0,i}) \times \prod_{j \in \mathcal{S}_i} \tilde{\mathcal{R}}_j^* \circ \tilde{\mathcal{D}}_j^j \mathbb{P}_k(\mathcal{T}_{\Gamma_j}) \right], \quad (31)$$

where  $\tilde{\mathcal{R}}_j^* : \mathbb{P}_k(\mathcal{T}_{\partial_j \Omega_j}) \rightarrow \mathbb{RT}_k(\mathcal{T}_{\Omega_j})$  is the discrete extension operator from internal boundary grids onto the interior of higher-dimensional subdomain grids, cf. [13] for a detailed discussion of the construction of this operator. We can now write the approximated dual weak problem as follows.

**Definition 11** (Approximated weak dual form on non-matching grids). *Let  $k \geq 0$  and  $\mathbf{u}_h = [\mathbf{u}_{h,0,i}, \lambda_{h,j}]$ ,  $p_h = [p_{h,i}]$ . Then, given  $f = [f_i] \in L^2(\Omega)$  and*

$g_D = [g_{D,i}] \in H^{1/2}(\partial_D\Omega)$ , find  $\mathbf{u}_h \in \mathbf{X}_k$  and  $p_h \in \mathbb{P}_k(\mathcal{T}_\Omega)$  such that

$$\begin{aligned} & \sum_{i \in I} \sum_{K \in \mathcal{T}_{\Omega_i}} \left( \mathcal{K}_i^{-1} \left( \mathbf{u}_{h,0,i} + \sum_{j \in \hat{S}_i} \tilde{\mathcal{R}}_j^* \circ \tilde{\mathcal{D}}_j^j \lambda_{h,j} \right), \mathbf{v}_{h,0,i} + \sum_{j \in \hat{S}_i} \tilde{\mathcal{R}}_j^* \circ \tilde{\mathcal{D}}_j^j \nu_{h,j} \right)_K \\ & - \sum_{i \in I} \sum_{K \in \mathcal{T}_{\Omega_i}} \left( p_{h,i}, \nabla_i \cdot \left( \mathbf{v}_{h,0,i} + \sum_{j \in \hat{S}_i} \tilde{\mathcal{R}}_j^* \circ \tilde{\mathcal{D}}_j^j \nu_{h,j} \right) + \sum_{j \in \hat{S}_i} \tilde{\mathcal{D}}_j^j \nu_{h,j} \right)_K \\ & + \sum_{j \in J} \sum_{K \in \mathcal{T}_{\Gamma_j}} \left( \kappa_j^{-1} \lambda_{h,j}, \nu_{h,j} \right)_K \\ & = - \sum_{i \in I} \sum_{K \in \mathcal{T}_{\partial_D\Omega_i}} \left( g_{D,i}, (\mathbf{v}_{h,0,i} \cdot \mathbf{n}_i)|_K \right)_K \quad \forall \mathbf{v}_h = [\mathbf{v}_{h,0,i}, \nu_{h,j}] \in \mathbf{X}_k. \end{aligned} \quad (32a)$$

$$\begin{aligned} & \sum_{i \in I} \sum_{K \in \mathcal{T}_{\Omega_i}} \left( \nabla_i \cdot \left( \mathbf{u}_{h,0,i} + \sum_{j \in \hat{S}_i} \tilde{\mathcal{R}}_j^* \circ \tilde{\mathcal{D}}_j^j \lambda_{h,j} \right), q_{h,i} \right)_K \\ & - \sum_{i \in I} \sum_{K \in \mathcal{T}_{\Omega_i}} \left( \sum_{j \in \hat{S}_i} \tilde{\mathcal{D}}_j^j \lambda_{h,j}, q_{h,i} \right)_K \\ & = \sum_{i \in I} \sum_{K \in \mathcal{T}_{\Omega_i}} \left( f_i, q_{h,i} \right)_K \quad \forall q_h = [q_{h,i}] \in \mathbb{P}_k(\mathcal{T}_\Omega). \end{aligned} \quad (32b)$$

In Definition 32, the Dirichlet boundary grid  $\mathcal{T}_{\partial_D\Omega_i}$  is defined in analogy to (4.1).

#### 4.4 Broken energy norms

To finalize the section, we write the equivalence between the continuous and broken energy norms. For any mD function  $q_h \in \mathbb{P}_k(\mathcal{T}_\Omega) \cap H_0^1(\Omega)$ ,  $k \geq 1$ , we define:

$$\| \| q_h \| \|^2 = \sum_{i \in I} \sum_{K \in \mathcal{T}_{\Omega_i}} \left\| \mathcal{K}_i^{1/2} \nabla_i q_{h,i} \right\|_K^2 + \sum_{j \in J} \sum_{K \in \mathcal{T}_{\Gamma_j}} \left\| \kappa_j^{1/2} \left( \tilde{\mathcal{P}}_j^j q_{h,j} - \tilde{\mathcal{P}}_j^j q_{h,j} \right) \right\|_K^2, \quad (33)$$

and for any mD function  $\mathbf{v}_h = [\mathbf{v}_{h,0,i}, \nu_{h,j}] \in \mathbf{X}_k$ ,  $k \geq 0$ , we define:

$$\| \| \mathbf{v}_h \| \|^2_* = \sum_{i \in I} \sum_{K \in \mathcal{T}_{\Omega_i}} \left\| \mathcal{K}_i^{-1/2} \left( \mathbf{v}_{h,0,i} + \sum_{j \in \hat{S}_i} \tilde{\mathcal{R}}_j^* \circ \tilde{\mathcal{D}}_j^j \nu_{h,j} \right) \right\|_K^2 + \sum_{j \in J} \sum_{K \in \mathcal{T}_{\Gamma_j}} \left\| \kappa_j^{-1/2} \nu_{h,j} \right\|_K^2. \quad (34)$$

## 5 A posteriori error estimation

In this section, we first present the abstract *a posteriori* error bounds for the case of non-matching grids. Then, after introducing the reconstruction of fluxes and potentials, we establish fully computable bounds for finite-element and mixed finite-element approximations.

## 5.1 A posteriori error estimates

Theorem 5.1 in [20] provides a general framework for a *a posteriori* error estimation in hierarchical mD elliptic problems. In this work, we focus on its application to locally mass-conservative approximations on non-matching grids, deriving explicit error bounds for the primal and dual variables. Before presenting the main theorem, we make explicit the local mass conservation property in the following assumption.

**Assumption 4** (Locally mass-conservative fluxes on non-matching grids). *Let  $\mathbf{u}_h = [\mathbf{u}_{h,0,i}, \lambda_{h,j}]$  be an approximated mD flux. We say  $\mathbf{u}_h$  is locally mass-conservative if for all  $K \in \mathcal{T}_{\Omega_i}$ ,  $i \in I$ , there holds*

$$\left( \nabla_i \cdot (\mathbf{u}_{h,0,i} + \sum_{j \in \hat{S}_i} \tilde{\mathcal{R}}_j^* \circ \tilde{\mathcal{D}}_j^j \lambda_{h,j}) - \sum_{j \in \hat{S}_i} \tilde{\mathcal{D}}_j^j \lambda_{h,j}, 1 \right)_K = (f_i, 1)_K. \quad (35)$$

Note that to satisfy Assumption 4 on non-matching grids, the discrete projection operators  $\tilde{\mathcal{D}}_j^j$  and  $\tilde{\mathcal{D}}_j^j$  (cf. Section 4.2.3) play a key role, as their construction guarantees inter-dimensional mass conservation. Dual approximations such as the one presented in Definition 32 naturally satisfy Assumption 4. However, primal approximations require more work. Usually, in a post-processing step, one has to locally equilibrate the fluxes to recover  $H(\text{div})$ -conformity (see, e.g., Section 5.2).

We are now ready to state the main theorem.

**Theorem 1** (Abstract *a posteriori* error estimates for locally mass-conservative fluxes on non-matching grids). *Define the error majorant  $\mathcal{M}^\oplus(q, \mathbf{v}, f)$ , valid for any  $q = [q_i] \in H_0^1(\Omega) + g$  and any  $\mathbf{v} = [\mathbf{v}_{0,i}, \nu_j] \in \mathbf{X}$  satisfying Assumption 4, as*

$$\mathcal{M}^\oplus(q, \mathbf{v}, f) := \eta_{\text{DF}}(q, \mathbf{v}) + \eta_{\text{R}}(\mathbf{v}, f), \quad (36)$$

where

$$\eta_{\text{DF}}^2(q, \mathbf{v}) = \sum_{i \in I} \sum_{K \in \mathcal{T}_{\Omega_i}} \eta_{\text{DF}\parallel, K}^2 + \sum_{j \in J} \sum_{K \in \mathcal{T}_{\Gamma_j}} \eta_{\text{DF}\perp, K}^2, \quad (37a)$$

$$\eta_{\text{R}}^2(\mathbf{v}, f) = \sum_{i \in I} \sum_{K \in \mathcal{T}_{\Omega_i}} \eta_{\text{R}, K}^2, \quad (37b)$$

are respectively the square of the global diffusive and residual errors, with

$$\eta_{\text{DF}\parallel, K} = \left\| \mathcal{K}^{-1/2} (\mathbf{v}_{0,i} + \sum_{j \in \hat{S}_i} \tilde{\mathcal{R}}_j^* \circ \tilde{\mathcal{D}}_j^j \nu_j) + \mathcal{K}^{1/2} \nabla_i q_i \right\|_K, \quad (38a)$$

$$\eta_{\text{DF}\perp, K} = \left\| \kappa_j^{-1/2} \nu_j + \kappa_j^{1/2} (\tilde{\mathcal{P}}_j^j q_j - \tilde{\mathcal{P}}_j^j q_j) \right\|_K, \quad (38b)$$

$$\eta_{\text{R}, K} = \frac{h_K}{\pi c_{\mathcal{K}_i, K}} \left\| f_i - \nabla \cdot (\mathbf{v}_{0,i} + \sum_{j \in \hat{S}_i} \tilde{\mathcal{R}}_j^* \circ \tilde{\mathcal{D}}_j^j \nu_j) + \sum_{j \in \hat{S}_i} \tilde{\mathcal{D}}_j^j \nu_j \right\|_K, \quad (38c)$$

respectively denoting the local subdomain diffusive, local interface diffusive, and local residual errors and with  $c_{\mathcal{K},K}$  denoting the smallest eigenvalue of the permeability matrix  $\mathcal{K}_i$  restricted to the element  $K$ . The following *a posteriori* error estimates hold:

(i) *Guaranteed upper bound for the primal mD variable.*

Let  $p = [p_i] \in H_0^1(\Omega) + g$  be the solution to the weak primal form from Definition 4 and  $q = [q_i] \in \mathbb{P}_k(\mathcal{T}_\Omega) \cap (H_0^1(\Omega) + g)$  for  $k \geq 1$  be arbitrary. Then, for any  $\mathbf{v} = [\mathbf{v}_{0,i}, \lambda_j] \in \mathbf{X}_k$  with  $k \geq 0$  satisfying Assumption 4, there holds

$$\|p - q\| \leq \mathcal{M}^\oplus(q, \mathbf{v}, f) =: \mathcal{M}_p^\oplus, \quad (39)$$

where  $\mathcal{M}_p^\oplus$  is the upper bound for the primal variable.

(ii) *Guaranteed upper bound for the dual mD variable.*

Let  $\mathbf{u} = [\mathbf{u}_{0,i}, \lambda_j] \in \mathbf{X}$  be the solution to the weak dual form from Definition 5 and  $\mathbf{v} = [\mathbf{v}_{0,i}, \nu_j] \in \mathbf{X}_k$  satisfying Assumption 4 with  $k \geq 0$  be arbitrary. Then, for any  $q = [q_i] \in \mathbb{P}_k(\mathcal{T}_\Omega) \cap H_0^1(\Omega) + g$  with  $k \geq 1$ , there holds

$$\|\mathbf{u} - \mathbf{v}\|_* \leq \mathcal{M}^\oplus(q, \mathbf{v}, f) =: \mathcal{M}_\mathbf{u}^\oplus, \quad (40)$$

where  $\mathcal{M}_\mathbf{u}^\oplus$  is the upper bound for the dual variable.

*Proof.* Due to the functional compatibility of the discrete projection operators introduced in Section 4.2, the proof is identical to the one presented in Appendix C from [20]. The proof combines techniques from *a posteriori* error estimates of the functional type [31, 32] and results from mD functional analysis [1].  $\square$

## 5.2 Conforming fluxes and potentials

In order to apply the *a posteriori* bounds from Theorem 1, we need an mD potential in  $H_0^1(\Omega) + g$  and an mD flux in  $\mathbf{X}$  that satisfies mass conservation at the element level. Approximations to the primal problem (Definition 10) only provide the first ingredient, whereas approximations to the dual problem (Definition 32) only provide the second ingredient. Thus, to obtain computable bounds using the finite element method one has to reconstruct the fluxes, while the mixed-finite element requires the reconstruction of the potentials. Deriving optimal reconstruction techniques, even in the lowest-order case, is non-trivial, as one has to balance accuracy with computational cost. We therefore maintain the definition of conforming fluxes and potentials as general as possible while providing references to guide the reader.

**Definition 12** (Conforming flux). *We define a conforming flux as any function  $\sigma_h$  that satisfies*

$$\sigma_h \in \mathbf{X}, \quad (41)$$

*and Assumption 4.*

Conforming fluxes are typically obtained after equilibrating the fluxes resulting of solving the discrete weak primal problem from Definition 10.

**Remark 9** (On flux reconstruction). *Classical flux reconstruction techniques include (i) superconvergent patch recovery [33, 34] with  $H(\text{div})$ -projections, (ii) local Neumann-patch solves [35–38], and (iii) hybrid explicit-recovery approaches [39]. In the  $mD$  setting, flux equilibration has been limited to enforcing mass balance across  $2D/1D$  matrix–fracture interfaces couplings [17, 18, 40]. To our knowledge, a general  $mD$  flux reconstruction framework has not yet been proposed.*

**Definition 13** (Conforming potential). *We define a conforming potential as any function  $s_h$  that satisfies*

$$s_h \in H_0^1(\Omega) + g. \quad (42)$$

**Remark 10** (On potential reconstruction). *Several techniques exist to recover continuous potentials from a non-conforming discretization in individual subdomains. Common approaches include: (i) patch-wise weighted average of cell-centered potentials (e.g., Green-Gauss, distance-weighted averages and least squares fits) [41–45], (ii) element-wise quadratic reconstruction via local polynomial solves [46, 47], and (iii) element-wise linear postprocessing based on lowest-order Raviart-Tomas basis functions [48]. Since the  $mD$  formulation does not require inter-dimensional continuity of potentials, any of these methods can be applied independently to each subdomain grid.*

### 5.3 Fully computable a posteriori error estimates

Computable estimates are now readily available for primal and dual approximations.

**Definition 14** (Computable bounds for finite element approximations). *Let  $p_h \in \mathbb{P}_k(\mathcal{T}_\Omega) \cap (H_0^1(\Omega) + g)$  with  $k \geq 1$  be the solution to the approximated primal problem from Definition 10, and  $\sigma_h \in \mathbf{X}_k$  for  $k \geq 0$  be a conforming flux (cf. Definition 12). Then, set  $q = p_h$  and  $\mathbf{v} = \sigma_h$  in Theorem 1 to obtain fully computable bounds.*

**Definition 15** (Computable bounds for mixed-finite element approximations). *Let  $(\mathbf{u}_h, p_h) \in (\mathbf{X}_k \times \mathbb{P}_k(\mathcal{T}_\Omega))$  with  $k \geq 0$  be the solution to the dual approximated problem from Definition 32, and let  $s_h \in \mathbb{P}_k(\mathcal{T}_\Omega) \cap H_0^1(\Omega) + g$  for  $k \geq 1$  be a conforming potential (cf. Definition 13). Then, set  $q = s_h$  and  $\mathbf{v} = \mathbf{u}_h$  in Theorem 1 to obtain fully computable bounds.*

Thanks to the functional-based construction of the abstract *a posteriori* error estimates and provided that approximated potentials and fluxes are properly reconstructed, other classical discretization techniques also fall within the

scope of application of Theorem 1. Important methods used in flow modeling in fractured porous media include the cell-centered finite volume method (CCFVM) [49, 50]—both the two-point flux approximation (TPFA) and the multi-point flux approximation (MPFA)—, the Vertex-Centered Finite Volume Method [51], the Mimetic Finite Difference Method [52, 53], the Discontinuous Galerkin Method [54, 55], and the Dual Mixed Virtual Element Method (MVEM) [12].

## 5.4 Error indicators

It is often desirable to associate error estimates to an entire subdomain or interface grid. To this aim, we introduce the following error indicators. Let  $\eta_{\text{DF}\parallel,K}$  and  $\eta_{\text{R},K}$  for  $K \in \mathcal{T}_{\Omega_i}$  and  $\eta_{\text{DF}\perp,K}$  for  $K \in \mathcal{T}_{\Gamma_j}$  be the local error estimators from Theorem 1. Then, we define the subdomain error indicator  $\eta_{\Omega_i}$  and the interface error indicator  $\eta_{\Gamma_j}$  as

$$\eta_{\Omega_i}^2 := \sum_{K \in \mathcal{T}_{\Omega_i}} \left( \eta_{\text{DF}\parallel,K}^2 + \eta_{\text{R},K}^2 \right) \quad \text{and} \quad \eta_{\Gamma_j}^2 := \sum_{K \in \mathcal{T}_{\Gamma_j}} \eta_{\text{DF}\perp,K}^2. \quad (43)$$

To report results of complex fracture networks, it is beneficial to aggregate subdomain and interface errors of the same dimensionality. Let  $I_{d_i} \subseteq I$  and  $J_{d_j} \subseteq J$  be the reduced index sets of subdomains and interfaces of dimension  $d_i$  and  $d_j$ , respectively. We shall then use

$$\eta_{\Omega^{d_i}}^2 := \sum_{i \in I_{d_i}} \eta_{\Omega_i}^2 \quad \text{and} \quad \eta_{\Gamma^{d_j}}^2 := \sum_{j \in J_{d_j}} \eta_{\Gamma_j}^2, \quad (44)$$

to designate the error indicators of all  $d_i$ -dimensional subdomains and all  $d_j$ -dimensional interfaces, respectively.

## 5.5 Effectivity indices

To quantify the efficiency of the *a posteriori* error estimates, we shall employ the following effectivity indices

$$I_p^{\text{eff}} = \frac{\mathcal{M}_p^\oplus(s_h, \sigma_h, f)}{\|p - s_h\|}, \quad I_{\mathbf{u}}^{\text{eff}} = \frac{\mathcal{M}_{\mathbf{u}}^\oplus(s_h, \sigma_h, f)}{\|\mathbf{u} - \sigma_h\|_*}. \quad (45)$$

## 6 Numerical examples

In this section, we present numerical verifications of the proposed non-matching error estimators against manufactured solutions and their application for test cases based on community benchmarks of flow in fractured porous media. For the sake of compactness, we only perform our analysis on mD domains with 3D hosts given that cases with 2D hosts are considerably less complex.

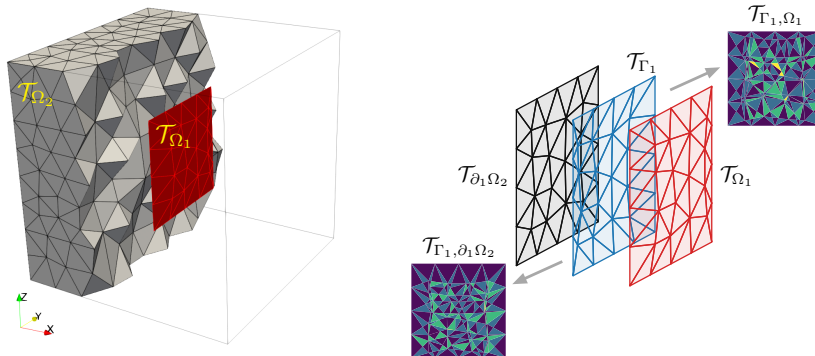


Figure 4: 3D/2D numerical verification setup. Left: Mixed-dimensional grid showcasing the matrix grid  $\mathcal{T}_{\Omega_2}$  and the fully embedded fracture grid  $\mathcal{T}_{\Omega_1}$ . Right: Exploded view of the non-matching coupling between  $\mathcal{T}_{\partial_1\Omega_2}$  (black),  $\mathcal{T}_{\Gamma_1}$  (blue), and  $\mathcal{T}_{\Omega_1}$  (red) with the corresponding transfer grids  $\mathcal{T}_{\Gamma_1, \partial_1\Omega_2}$  and  $\mathcal{T}_{\Gamma_1, \Omega_1}$  (triangles are colored for visualization purposes only). Example shown for  $h = 0.15$  and translation  $+\mathbf{e}_y$ .

To obtain the numerical approximations, we employ the MPFA method [25, 49, 50], which is closely related to the lowest-order mixed-finite element approximation [56]. Fully computable estimates are obtained after two postprocessing steps:

- (i) MPFA face fluxes are directly mapped to the coefficients of the local RT0 space (guaranteeing continuity of normal traces) [41]. Repeating this process in each subdomain grid yields a conforming mD flux  $\sigma_h \in \mathbf{X}_0$  (cf. Definition 12).
- (ii) MPFA potentials are reconstructed in each subdomain grid to obtain a conforming mD potential  $s_h \in \mathbb{P}_1(\mathcal{T}_\Omega) \cap H_0^1(\Omega) + g$  using the potential reconstruction technique proposed in [48]. The technique employs the local MPFA face fluxes to first approximate a cell-centered potential gradient at the cell's barycenter which is then mapped to the cell vertices and added to the cell-center potential. This process produces  $\mathbb{P}_1$ -nodal potentials which are generally non-conforming. Thus, the Oswald interpolator is applied as a final step to produce a conforming global linear potential  $s_h \in H_0^1(\Omega) + g$  (cf. Definition 13).

All numerical examples were implemented in `PorePy` [25] and are available for reproduction through the extension package `mdnme` [57].

## 6.1 3D/2D verification with a manufactured solution

We employ the 3D manufactured solution from Section 7 of [20] to verify the efficiency of our non-matching error estimators. The mD domain consists of a

unit cube  $\Omega_2 = (0, 1)^3$  hosting a fully embedded vertical fracture

$$\Omega_1 = \{(x, y, z) \in \mathbb{R}^3 : x = 0.5, 0.25 \leq y \leq 0.75, 0.25 \leq z \leq 0.75\}.$$

Interfaces  $\Gamma_1$  and  $\Gamma_2$  couple  $\Omega_2$  to the left and right sides of  $\Omega_1$ , respectively (see Fig. 4). With a smooth matrix pressure  $p_2 : \Omega_2 \rightarrow \mathbb{R}$ , unit tangential permeabilities  $\mathcal{K}_2 = \mathbf{I}_{3 \times 3}$  and  $\mathcal{K}_1 = \mathbf{I}_{2 \times 2}$ , the exact Darcy fluxes  $\mathbf{u}_2 : \Omega_2 \rightarrow \mathbb{R}^3$  and  $\mathbf{u}_1 : \Omega_1 \rightarrow \mathbb{R}^2$  follow from (2b). With unit normal permeabilities  $\kappa_1 = \kappa_2 = 1$ , the interface fluxes  $\lambda_1 : \Gamma_1 \rightarrow \mathbb{R}$  and  $\lambda_2 : \Gamma_2 \rightarrow \mathbb{R}$  follow from (2c). Finally, (2a) gives the exact sources  $f_2 : \Omega_2 \rightarrow \mathbb{R}$  and  $f_1 : \Omega_1 \rightarrow \mathbb{R}$ . Exact expressions are listed in Appendix D.2 of [20].

We consider four refinement levels with target mesh sizes  $h \in \{0.3, 0.15, 0.075, 0.0375\}$ . For each  $h$ , we first build a fully matching tessellation of the mD grid (reference configuration). From this, we generate non-matching grids by systematically perturbing internal nodes of the fracture grid  $\mathcal{T}_{\Omega_1}$  and the interface side grids  $\mathcal{T}_{\Gamma_1}$  and  $\mathcal{T}_{\Gamma_2}$ . Concretely, each internal node of  $\mathcal{T}_{\Omega_1}$  is translated by half of the grid’s mean cell diameter in the eight in-plane directions  $\{\pm \mathbf{e}_y, \pm \mathbf{e}_z, \pm(\mathbf{e}_y + \mathbf{e}_z), \pm(\mathbf{e}_y - \mathbf{e}_z)\}$ , while internal nodes of  $\mathcal{T}_{\Gamma_1}$  and  $\mathcal{T}_{\Gamma_2}$  are perturbed in the opposite directions (same magnitude). Nodes of the internal boundary grids  $\mathcal{T}_{\partial_1 \Omega_2}$  and  $\mathcal{T}_{\partial_2 \Omega_2}$  are left unperturbed. This procedure yields eight fully non-matching configurations per  $h$ ; see the right panel of Fig. 4 for the left non-matching coupling corresponding to  $h = 0.15$  and  $+\mathbf{e}_y$  perturbation direction.

Tables 2 and 3 report, respectively, the majorants, true errors, and effectivity indices, and the subdomain/interface contributions, for both matching and non-matching cases. For non-matching results we show the mean over the eight perturbations together with the sample standard deviation. The results indicate that (i) the majorants and effectivity indices for the primal and dual variables remain close to the matching baseline, and (ii) the subdomain and interface contributions decrease monotonically with refinement. The tested non-matching couplings are deliberately challenging (fully non-matching with finite perturbations) to stress-test the estimators; in applications, controlled refinement typically leads to even milder mismatches.

## 6.2 Regular fracture network

This numerical example employs the setup of Case 2: Regular network, from the 3D flow benchmark [7]. The mD domain consists of a unit cube matrix hosting nine regularly oriented fractures (see the left panel of Fig. 5), resulting in an mD domain with one 3D subdomain, nine 2D subdomains, sixty-nine 1D subdomains, and twenty-seven 0D intersection points.

The original benchmark prescribes no-flux boundary conditions in all external faces except on the red and blue regions, where a constant Darcy flux ( $\mathbf{u} = -1$ ) and a constant pressure ( $p = 1$ ) are imposed, respectively. Since our theory does not cover non-zero external boundary fluxes, and following [20], we replace the inflow Neumann condition by a Dirichlet condition with  $p = 1$  and set the outlet pressure to  $p = 0$ . The matrix subdomain is assigned permeability

Table 2: 3D/2D verification results: majorants, true errors and effectivity indices.

$h$	$\mathcal{M}_p^\oplus = \mathcal{M}_u^\oplus$	$\ \mathbf{u} - \boldsymbol{\sigma}_h\ _*$	$I_u^{\text{eff}}$	$\ p - s_h\ $	$I_p^{\text{eff}}$
0.3	2.69e-1	7.10e-2	3.78	2.34e-1	1.15
	$2.70\text{e-}1 \pm 1.34\text{e-}3$	$7.06\text{e-}2 \pm 4.29\text{e-}4$	$3.83 \pm 2.0\text{e-}2$	$2.36\text{e-}1 \pm 6.07\text{e-}4$	$1.15 \pm 4.6\text{e-}3$
0.15	1.76e-1	4.56e-2	3.86	1.60e-1	1.10
	$1.77\text{e-}1 \pm 4.20\text{e-}4$	$4.63\text{e-}2 \pm 7.99\text{e-}4$	$3.81 \pm 5.7\text{e-}2$	$1.60 \pm 3.17\text{e-}4$	$1.10 \pm 6.0\text{e-}4$
0.075	9.28e-2	2.78e-2	3.34	8.48e-2	1.09
	$9.33\text{e-}2 \pm 3.04\text{e-}4$	$2.90\text{e-}2 \pm 1.32\text{e-}3$	$3.22 \pm 1.4\text{e-}1$	$8.54\text{e-}2 \pm 5.31\text{e-}4$	$1.09 \pm 3.3\text{e-}3$
0.0375	4.75e-2	1.86e-2	2.56	4.59e-2	1.04
	$4.77\text{e-}2 \pm 2.11\text{e-}4$	$1.64\text{e-}2 \pm 2.37\text{e-}3$	$2.96 \pm 4.2\text{e-}1$	$4.51\text{e-}2 \pm 8.78\text{e-}4$	$1.06 \pm 1.6\text{e-}2$

Table 3: 3D/2D verification results: Subdomain and interface errors.

$h$	$\eta_{\Omega_2}$	$\eta_{\Omega_1}$	$\eta_{\Gamma_1}$	$\eta_{\Gamma_2}$
0.3	2.43e-1	8.37e-3	6.26e-3	6.18e-3
	$2.43\text{e-}1 \pm 1.87\text{e-}4$	$5.47\text{e-}3 \pm 5.83\text{e-}3$	$2.28\text{e-}2 \pm 4.91\text{e-}3$	$2.24\text{e-}2 \pm 4.13\text{e-}3$
0.15	1.66e-1	1.62e-5	1.35e-3	1.35e-3
	$1.66\text{e-}1 \pm 8.33\text{e-}5$	$3.20\text{e-}3 \pm 3.44\text{e-}3$	$5.77\text{e-}3 \pm 1.17\text{e-}3$	$5.47\text{e-}3 \pm 1.01\text{e-}3$
0.075	8.90e-2	1.06e-5	3.89e-4	3.88e-4
	$8.91\text{e-}2 \pm 7.05\text{e-}5$	$1.81\text{e-}3 \pm 1.92\text{e-}3$	$4.61\text{e-}3 \pm 1.12\text{e-}3$	$4.52\text{e-}3 \pm 1.16\text{e-}3$
0.0375	4.65e-2	1.43e-3	1.13e-4	1.15e-4
	$4.64\text{e-}2 \pm 3.53\text{e-}5$	$8.58\text{e-}4 \pm 9.14\text{e-}4$	$2.31\text{e-}3 \pm 1.45\text{e-}3$	$2.33\text{e-}3 \pm 1.40\text{e-}3$

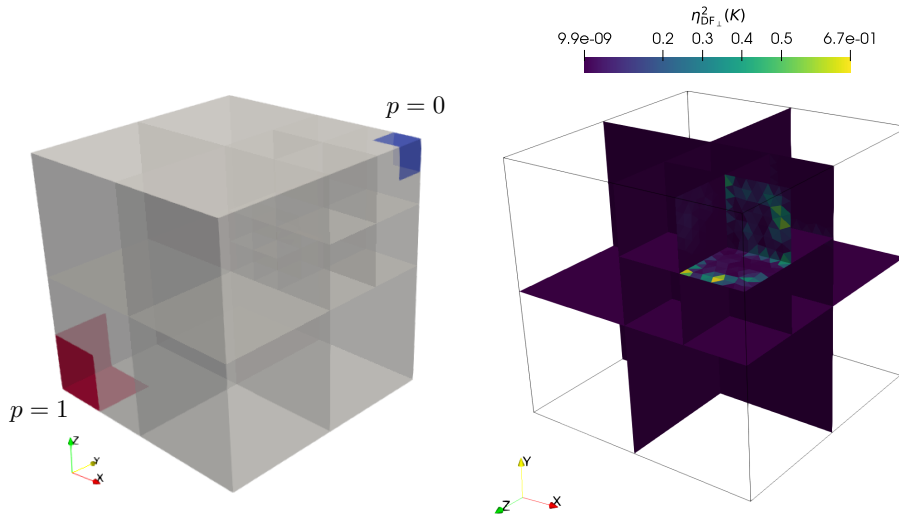


Figure 5: Regular network. Left: Geometry of the fracture network and boundary conditions. Right: Local diffusive error estimators of 2D interface grids for the finest mesh resolution.

values  $\mathcal{K} \in \{1, 0.1\}$ , while the fractures are considered conductive ( $\mathcal{K} = 1 \times 10^4$ ). The complete set of parameters can be found in Table 4 from [7].

The benchmark employs three levels of refinement, with approximately 500, 1 400 and 32 000 three-dimensional cells. To generate the non-matching grids, we begin from a fully matching tessellation of the mD domain and then globally refine all fracture grids using nested bisection [58]. Importantly, we do not refine the 1D subdomains grids. Refining 1D subdomain grids increases the resolution around intersection points—well-known points of singularity—without improving the accuracy of interface fluxes, resulting in a larger mismatch between the interface fluxes and the (permeability-scaled) pressure jumps (2c). We emphasize that this phenomenon is related to the limited regularity of the model itself [3], rather to any deficiency of the error estimators.

Table 4 reports the aggregated local errors grouped by dimensionality, together with the majorant. All quantities decrease monotonically with refinement, as expected for a stable and consistent numerical scheme. The dominant contributions to the majorant originate from the 2D interfaces, highlighting that MPFA struggles to accurately represent the interface law; this is expected considering that it is a lowest-order method. The right panel of Fig. 5 shows the spatial distribution of the local diffusive errors. Not surprisingly, the largest errors are located around the outlet boundary region, where steep pressure gradients occur.

Table 4: Majorant and dimension-based aggregated error estimators for the 3D regular network benchmark from Section 6.2.

Mesh	$\eta_{\Omega^3}$	$\eta_{\Omega^2}$	$\eta_{\Omega^1}$	$\eta_{\Gamma^2}$	$\eta_{\Gamma^1}$	$\eta_{\Gamma^0}$	$\mathcal{M}^\oplus$
Coarse	5.70e-1	3.56e-2	1.16e-3	4.35e+2	4.27e+0	8.29e-2	1.98e+2
Intermediate	3.80e-1	1.92e-2	8.71e-4	6.57e+1	3.19e+0	2.32e-2	2.60e+1
Fine	3.24e-1	1.10e-2	6.95e-4	1.52e+1	1.41e+0	1.51e-2	6.55e+0

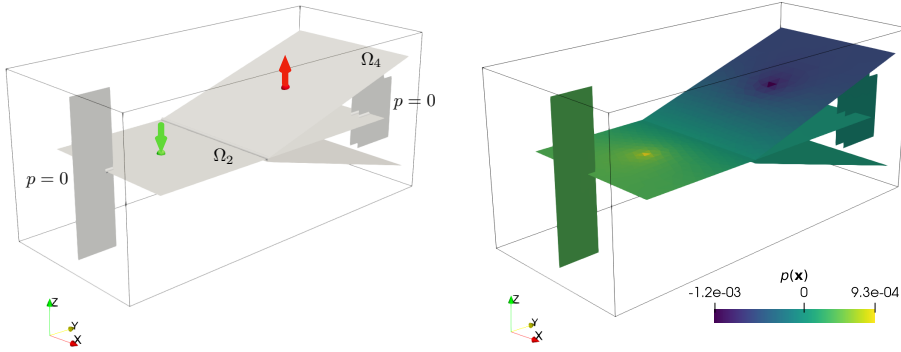


Figure 6: Network with small features. Left: Geometry, boundary conditions, and source/sink locations. Right: Resulting pressure distribution (shown only on 2D subdomains for visualization).

### 6.3 Production on a fracture network with small features

In this numerical example, we consider the setup of Case 3: Network with small features from the 3D verification benchmark [7] to analyze non-matching approximations of an idealized injection/production scenario. To reduce the influence of boundary conditions on the error estimates, we modify the original specification (cf. Section 5.3 of [7]) and impose no-flux boundary conditions on all boundaries except the South and North faces, where we prescribe a constant Dirichlet condition  $p = 0$ ; see the left panel of Fig. 6. We then add an injection well on  $\Omega_2$  and a production well on  $\Omega_4$ , modeled as constant source terms on the well cells:

$$f_2(\mathbf{x}) = \begin{cases} 0.1, & \mathbf{x} = (0.5, 0.65, 0.5) \\ 0, & \text{elsewhere} \end{cases} \quad \text{and} \quad f_4(\mathbf{x}) = \begin{cases} -0.1, & \mathbf{x} = (0.5, 1.6, 0.675) \\ 0, & \text{elsewhere} \end{cases},$$

where the conditions on  $\mathbf{x}$  imply the cell containing said coordinate. Following the benchmark, we assign unitary permeability in the matrix  $\mathcal{K} = 1$  and  $\mathcal{K} = 1 \times 10^4$  in the fractures, while the remaining material parameters are taken from Table 5 of [7]. The resulting pressure distribution is shown in the right panel of Fig. 6.

Table 5: Majorant and dimension-based aggregated error estimators for the 3D fracture network with small features from Section 6.3.

Approximation	$\eta_{\Omega^3}$	$\eta_{\Omega^2}$	$\eta_{\Omega^1}$	$\eta_{\Gamma^2}$	$\eta_{\Gamma^1}$	$\mathcal{M}^\oplus$
Matching	8.06e-4	8.14e-3	4.96e-6	2.68e-1	2.04e-4	1.24e-1
Non-matching	8.88e-4	8.11e-3	4.56e-6	2.71e-1	1.30e-4	1.26e-1

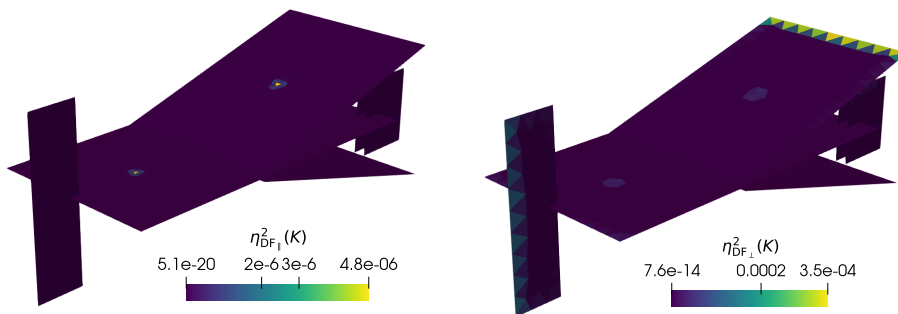


Figure 7: Non-matching local error estimators for the 3D fracture network with small features. Left: 2D diffusive errors on subdomains. Right: 2D diffusive errors on interfaces.

In contrast to the previous numerical example, our goal here is not to perform a full convergence study, but to compare matching and non-matching approximations. As before, the non-matching mD grid is constructed by bisecting the matching mD grid and replacing the finer fracture grids into the coarser mD grid.

Table 5 shows the aggregated error contributions for both discretizations. The non-matching estimators closely reproduce the matching ones, with differences at most a few percent and a relative deviation of approximately 1.2% in the majorant. The non-matching approximation yields slightly larger contributions in the 3D subdomain and in the 2D interfaces, and slightly smaller contributions in the 2D and 1D subdomains as well as in the 1D interfaces. This illustrates the subtlety of non-matching refinement in mD geometries: refining fractures without fully refining interfaces may reduce errors in some components while increasing them in others. Moreover, the interface grid cannot be refined freely without simultaneously refining its adjacent internal boundary grid, as this may violate inf-sup stability conditions [13, 24]. Finally, it is important to remark that the residual contributions vanish for both approximations due to the local mass-conservative properties of MPFA [20].

Figure 7 shows the spatial distribution of the 2D subdomain and interface diffusive errors for the non-matching approximation. As expected, the largest subdomain errors occur near the injection and production wells. In contrast, the interface errors are primarily concentrated along the fracture boundaries,

which are known to be challenging regions for mD flow discretizations.

## 7 Conclusion

In this article, we have extended the *a posteriori* error estimators developed in [20] for matching grids to the setting of non-matching mD discretizations for elliptic problems, with particular emphasis on single-phase flow in fractured porous media. Using postprocessed MPFA approximations, we verified the validity of the proposed non-matching estimators—and, consequently, of the underlying discrete projection operators—on synthetic test cases with exact solutions as well as on 3D community benchmark problems featuring complex geometries and realistic material-parameter contrasts. The results confirm that the estimators remain reliable under non-matching refinement, while simultaneously highlighting the delicate interplay between accuracy, refinement choices, and stability requirements in mD settings.

## Acknowledgments

This project has received funding from the European Research Council (ERC) under the European Union’s Horizon 2020 research and innovation programme (grant agreement No 101002507). JV was funded by the Paraguayan National Council of Science and Technology (CONACYT) through the program: Advanced Human Capital Insertion in Academia (PRIA01-8). CES was funded by CONACYT project number ESTR01-23 and by SISNI. The authors would like to thank Jan M. Nordbotten for valuable discussions on the topic.

## References

- [1] W. M. Boon, J. M. Nordbotten, and J. E. Vatne. Functional analysis and exterior calculus on mixed-dimensional geometries. *Annali di Matematica Pura ed Applicata (1923-)*, page 757–789, 2021. doi: [10.1007/s10231-020-01013-1](https://doi.org/10.1007/s10231-020-01013-1).
- [2] V. Martin, J. Jaffré, and J. E. Roberts. Modeling fractures and barriers as interfaces for flow in porous media. *SIAM J. Sci. Comput.*, 26(5):1667–1691, 2005. ISSN 1064-8275. doi: [10.1137/S1064827503429363](https://doi.org/10.1137/S1064827503429363).
- [3] J. M. Nordbotten, W. M. Boon, A. Fumagalli, and E. Keilegavlen. Unified approach to discretization of flow in fractured porous media. *Comput. Geosci.*, 23(2):225–237, 2019. ISSN 1420-0597. doi: [10.1007/s10596-018-9778-9](https://doi.org/10.1007/s10596-018-9778-9).
- [4] Inga Berre, Florian Doster, and Eirik Keilegavlen. Flow in fractured porous media: A review of conceptual models and discretization approaches.

- Transport in Porous Media*, 130(1):215–236, 2019. doi: [10.1007/s11242-018-1171-6](https://doi.org/10.1007/s11242-018-1171-6).
- [5] Luca Formaggia, Alessio Fumagalli, and Anna Scotti. *Numerical Methods for Flow in Fractured Porous Media*, pages 1125–1130. Springer International Publishing, Cham, 2021. ISBN 978-3-030-58631-7. doi: [10.1007/978-3-030-58631-7\\_289](https://doi.org/10.1007/978-3-030-58631-7_289). URL [https://doi.org/10.1007/978-3-030-58631-7\\_289](https://doi.org/10.1007/978-3-030-58631-7_289).
- [6] B. Flemisch, I. Berre, W. Boon, A. Fumagalli, N. Schwenck, A. Scotti, I. Stefansson, and A. Tatomir. Benchmarks for single-phase flow in fractured porous media. *Advances in Water Resources*, 111:239–258, 2018. doi: [10.1016/j.advwatres.2017.10.036](https://doi.org/10.1016/j.advwatres.2017.10.036).
- [7] I. Berre, W. M. Boon, B. Flemisch, A. Fumagalli, D. Gläser, E. Keilegavlen, A. Scotti, I. Stefansson, A. Tatomir, K. Brenner, S. Burbulla, P. Devloo, O. Duran, M. Favino, J. Hennicker, I-H. Lee, K. Lipnikov, R. Masson, K. Mosthaf, M. G. C. Nestola, C-F. Ni, K. Nikitin, P. Schädle, D. Svyatskiy, R. Yanbarisov, and P. Zulian. Verification benchmarks for single-phase flow in three-dimensional fractured porous media. *Advances in Water Resources*, 147:103759, 2021. ISSN 0309-1708. doi: [10.1016/j.advwatres.2020.103759](https://doi.org/10.1016/j.advwatres.2020.103759).
- [8] Jakub Wiktor Both, Bergit Brattekkås, Eirik Keilegavlen, Martin Fernø, and Jan Martin Nordbotten. High-fidelity experimental model verification for flow in fractured porous media. *InterPore Journal*, 1(3):IPJ271124–6, Nov. 2024. doi: [10.69631/ipj.v1i3nr31](https://doi.org/10.69631/ipj.v1i3nr31). URL <https://ipjournal.interpore.org/index.php/interpore/article/view/31>.
- [9] N. Frih, V. Martin, J. E. Roberts, and A. Saâda. Modeling fractures as interfaces with nonmatching grids. *Computational Geosciences*, 16(4):1043–1060, 2012. doi: [10.1007/s10596-012-9302-6](https://doi.org/10.1007/s10596-012-9302-6).
- [10] C. D’Angelo and A. Scotti. A mixed finite element method for darcy flow in fractured porous media with non-matching grids. *ESAIM: Mathematical Modelling and Numerical Analysis - Modélisation Mathématique et Analyse Numérique*, 46(2):465–489, 2012. doi: [10.1051/m2an/20111148](https://doi.org/10.1051/m2an/20111148).
- [11] Alessio Fumagalli and Anna Scotti. A numerical method for two-phase flow in fractured porous media with non-matching grids. *Advances in Water Resources*, 62:454–464, 2013. ISSN 0309-1708. doi: <https://doi.org/10.1016/j.advwatres.2013.04.001>. URL <https://www.sciencedirect.com/science/article/pii/S0309170813000523>. Computational Methods in Geologic CO2 Sequestration.
- [12] A. Fumagalli and E. Keilegavlen. Dual virtual element methods for discrete fracture matrix models. *Oil & Gas Science and Technology—Revue d’IFP Energies nouvelles*, 74:41, 2019. doi: [10.2516/ogst/2019008](https://doi.org/10.2516/ogst/2019008).

- [13] Wietse M. Boon, Dennis Gläser, Rainer Helmig, and Ivan Yotov. Flux-mortar mixed finite element methods on nonmatching grids. *SIAM Journal on Numerical Analysis*, 60(3):1193–1225, 2022. doi: [10.1137/20M1361407](https://doi.org/10.1137/20M1361407). URL <https://doi.org/10.1137/20M1361407>.
- [14] G. V. Pencheva, M. Vohralík, M. F. Wheeler, and T. Wildey. Robust a posteriori error control and adaptivity for multiscale, multinumercs, and mortar coupling. *SIAM J. Numer. Anal.*, 51(1):526–554, 2013. ISSN 0036-1429. doi: [10.1137/110839047](https://doi.org/10.1137/110839047).
- [15] Huangxin Chen, Amgad Salama, and Shuyu Sun. Adaptive mixed finite element methods for darcy flow in fractured porous media. *Water Resources Research*, 52(10):7851–7868, 2016. doi: [10.1002/2015WR018450](https://doi.org/10.1002/2015WR018450).
- [16] Huangxin Chen and Shuyu Sun. A residual-based a posteriori error estimator for single-phase darcy flow in fractured porous media. *Numerische Mathematik*, 136(3):805–839, 2017. doi: [10.1007/s00211-016-0851-9](https://doi.org/10.1007/s00211-016-0851-9).
- [17] Z. Mghazli and I. Naji. Guaranteed a posteriori error estimates for a fractured porous medium. *Math. Comput. Simulation*, 164:163–179, 2019. ISSN 0378-4754. doi: [10.1016/j.matcom.2019.02.002](https://doi.org/10.1016/j.matcom.2019.02.002).
- [18] F. Hecht, Z. Mghazli, I. Naji, and J. E. Roberts. A residual a posteriori error estimators for a model for flow in porous media with fractures. *J. Sci. Comput.*, 79(2):935–968, 2019. ISSN 0885-7474. doi: [10.1007/s10915-018-0875-7](https://doi.org/10.1007/s10915-018-0875-7).
- [19] Lina Zhao and Eric Chung. An adaptive discontinuous galerkin method for the Darcy system in fractured porous media. *Computational Geosciences*, 26(6):1581–1596, 2022. doi: [10.1007/s10596-022-10171-5](https://doi.org/10.1007/s10596-022-10171-5).
- [20] Jhabriel Varela, Elyes Ahmed, Eirik Keilegavlen, Jan M Nordbotten, and Florin A Radu. A posteriori error estimates for hierarchical mixed-dimensional elliptic equations. *Journal of Numerical Mathematics*, 31(4): 247–280, 2023. doi: [10.1515/jnma-2022-0038](https://doi.org/10.1515/jnma-2022-0038).
- [21] Martin J. Gander and Caroline Japhet. An algorithm for non-matching grid projections with linear complexity. In Michel Bercovier, Martin J. Gander, Ralf Kornhuber, and Olof Widlund, editors, *Domain Decomposition Methods in Science and Engineering XVIII*, pages 185–192. Springer Berlin Heidelberg, Berlin, Heidelberg, 2009. ISBN 978-3-642-02677-5. doi: [10.1007/978-3-642-02677-5\\_19](https://doi.org/10.1007/978-3-642-02677-5_19).
- [22] Martin J Gander and Caroline Japhet. Algorithm 932: PANG: software for nonmatching grid projections in 2D and 3D with linear complexity. *ACM Transactions on Mathematical Software (TOMS)*, 40(1):1–25, 2013. doi: [10.1145/2513109.2513115](https://doi.org/10.1145/2513109.2513115).

- [23] Conor McCoid and Martin J Gander. A provably robust algorithm for triangle-triangle intersections in floating-point arithmetic. *ACM Transactions on Mathematical Software (TOMS)*, 48(2):1–30, 2022. doi: [10.1145/3513264](https://doi.org/10.1145/3513264).
- [24] W. M. Boon, J. M. Nordbotten, and I. Yotov. Robust discretization of flow in fractured porous media. *SIAM J. Numer. Anal.*, 56(4):2203–2233, 2018. ISSN 0036-1429. doi: [10.1137/17M1139102](https://doi.org/10.1137/17M1139102).
- [25] E. Keilegavlen, R. Berge, A. Fumagalli, M. Starnoni, I. Stefansson, J. Varela, and I. Berre. Porepy: An open-source software for simulation of multiphysics processes in fractured porous media. *Computational Geosciences*, 25(1):243–265, 2021. doi: [10.1007/s10596-020-10002-5](https://doi.org/10.1007/s10596-020-10002-5).
- [26] Lawrence C. Evans. *Partial Differential Equations*, volume 19 of *Graduate Studies in Mathematics*. American Mathematical Society, Providence, RI, 2 edition, 2022. ISBN 978-1-4704-6765-9.
- [27] L Ridgway Scott and Shangyou Zhang. Finite element interpolation of nonsmooth functions satisfying boundary conditions. *Mathematics of computation*, 54(190):483–493, 1990. doi: [10.2307/2008497](https://doi.org/10.2307/2008497).
- [28] Jacques-Louis Lions and Enrico Magenes. *Non-Homogeneous Boundary Value Problems and Applications. Vol. 1*. Springer, Berlin, 2012. ISBN 978-3-642-65166-0.
- [29] William McLean. *Strongly Elliptic Systems and Boundary Integral Equations*, volume 131 of *Cambridge Studies in Advanced Mathematics*. Cambridge University Press, Cambridge, 2000. ISBN 978-0-521-63218-5.
- [30] Susanne C. Brenner and L. Ridgway Scott. *The Mathematical Theory of Finite Element Methods*, volume 15 of *Texts in Applied Mathematics*. Springer, New York, 3 edition, 2008. ISBN 978-0-387-75933-3.
- [31] S. I. Repin, S. Sauter, and A. Smolianski. Two-sided a posteriori error estimates for mixed formulations of elliptic problems. *SIAM J. Numer. Anal.*, 45(3):928–945, 2007. ISSN 0036-1429. doi: [10.1137/050641533](https://doi.org/10.1137/050641533).
- [32] S. I. Repin. *A posteriori estimates for partial differential equations*, volume 4 of *Radon Series on Computational and Applied Mathematics*. Walter de Gruyter GmbH & Co. KG, Berlin, 2008. ISBN 978-3-11-019153-0. doi: [10.1515/9783110203042](https://doi.org/10.1515/9783110203042).
- [33] O. C. Zienkiewicz and J. Z. Zhu. A simple error estimator and adaptive procedure for practical engineering analysis. *Internat. J. Numer. Methods Engrg.*, 24(2):337–357, 1987. ISSN 0029-5981. doi: [10.1002/nme.1620240206](https://doi.org/10.1002/nme.1620240206).
- [34] Olgierd Cecil Zienkiewicz and Jian Zhong Zhu. The superconvergent patch recovery and a posteriori error estimates. Part 1: The recovery technique. *International Journal for Numerical Methods in Engineering*, 33(7):1331–1364, 1992. doi: [10.1002/nme.1620330702](https://doi.org/10.1002/nme.1620330702).

- [35] Mark Ainsworth and J Tinsley Oden. A posteriori error estimators for second order elliptic systems. Part 2: An optimal order process for calculating self-equilibrating fluxes. *Computers & Mathematics with Applications*, 26(9):75–87, 1993. doi: [10.1016/0898-1221\(93\)90007-I](https://doi.org/10.1016/0898-1221(93)90007-I).
- [36] A. Ern and M. Vohralík. Polynomial-degree-robust a posteriori estimates in a unified setting for conforming, nonconforming, discontinuous Galerkin, and mixed discretizations. *SIAM J. Numer. Anal.*, 53(2):1058–1081, 2015. ISSN 0036-1429. doi: [10.1137/130950100](https://doi.org/10.1137/130950100).
- [37] Iain Smears and Martin Vohralík. Simple and robust equilibrated flux a posteriori estimates for singularly perturbed reaction–diffusion problems. *ESAIM: Mathematical Modelling and Numerical Analysis*, 54(6):1951–1973, 2020. doi: [10.1051/m2an/2020034](https://doi.org/10.1051/m2an/2020034).
- [38] Difeng Cai, Zhiqiang Cai, and Shun Zhang. Robust equilibrated a posteriori error estimator for higher order finite element approximations to diffusion problems. *Numerische Mathematik*, 144(1):1–21, 2020. doi: [10.1007/s00211-019-01075-1](https://doi.org/10.1007/s00211-019-01075-1).
- [39] Difeng Cai and Zhiqiang Cai. A hybrid a posteriori error estimator for conforming finite element approximations. *Computer Methods in Applied Mechanics and Engineering*, 339:320–340, 2018. doi: [10.1016/j.cma.2018.04.050](https://doi.org/10.1016/j.cma.2018.04.050).
- [40] H. Chen and S. Sun. A residual-based a posteriori error estimator for single-phase Darcy flow in fractured porous media. *Numer. Math.*, 136(3): 805–839, 2017. ISSN 0029-599X. doi: [10.1007/s00211-016-0851-9](https://doi.org/10.1007/s00211-016-0851-9).
- [41] S. Cochez-Dhondt, S. Nicaise, and S. I. Repin. A posteriori error estimates for finite volume approximations. *Math. Model. Nat. Phenom.*, 4(1):106–122, 2009. ISSN 0973-5348. doi: [10.1051/mmnp/20094105](https://doi.org/10.1051/mmnp/20094105).
- [42] Nianhua Wang, Ming Li, Rong Ma, and Laiping Zhang. Accuracy analysis of gradient reconstruction on isotropic unstructured meshes and its effects on inviscid flow simulation. *Advances in aerodynamics*, 1:1–31, 2019. doi: [10.1186/s42774-019-0020-9](https://doi.org/10.1186/s42774-019-0020-9).
- [43] Yunqing Huang, Kai Jiang, and Nianyu Yi. Some weighted averaging methods for gradient recovery. *Advances in Applied Mathematics and Mechanics*, 4(2):131–155, 2012. doi: [10.4208/aamm.10-m1188](https://doi.org/10.4208/aamm.10-m1188).
- [44] Emre Sozer, Christoph Brehm, and Cetin C Kiris. Gradient calculation methods on arbitrary polyhedral unstructured meshes for cell-centered CFD solvers. In *52nd Aerospace Sciences Meeting*, page 1440, 2014. doi: [10.2514/6.2014-1440](https://doi.org/10.2514/6.2014-1440).
- [45] Dimitri Mavriplis. Revisiting the least-squares procedure for gradient reconstruction on unstructured meshes. In *16th AIAA computational fluid dynamics conference*, page 3986, 2003. doi: [10.2514/6.2003-3986](https://doi.org/10.2514/6.2003-3986).

- [46] M. Vohralík. A posteriori error estimates for finite volume and mixed finite element discretizations of convection-diffusion-reaction equations. In *Paris-Sud Working Group on Modelling and Scientific Computing 2006–2007*, volume 18 of *ESAIM Proc.*, pages 57–69. EDP Sci., Les Ulis, 2007. doi: [10.1051/proc:071806](https://doi.org/10.1051/proc:071806).
- [47] M. Vohralík. Unified primal formulation-based a priori and a posteriori error analysis of mixed finite element methods. *Math. Comp.*, 79(272): 2001–2032, 2010. ISSN 0025-5718. doi: [10.1090/S0025-5718-2010-02375-0](https://doi.org/10.1090/S0025-5718-2010-02375-0).
- [48] Jhabriel Varela, Christian E. Schaerer, and Eirik Keilegavlen. A linear potential reconstruction technique based on Raviart–Thomas basis functions for cell-centered finite volume approximations to the Darcy problem. In *Proceeding Series of the Brazilian Society of Computational and Applied Mathematics*, volume 11, 2025. doi: [10.5540/03.2025.011.01.0332](https://doi.org/10.5540/03.2025.011.01.0332).
- [49] I. Aavatsmark. An introduction to multipoint flux approximations for quadrilateral grids. *Comput. Geosci.*, 6(3-4):405–432, 2002. ISSN 1420-0597. doi: [10.1023/A:1021291114475](https://doi.org/10.1023/A:1021291114475). Locally conservative numerical methods for flow in porous media.
- [50] Jan Martin Nordbotten and Eirik Keilegavlen. An introduction to multipoint flux (MPFA) and stress (MPSA) finite volume methods for thermo-poroelasticity. In Daniele Antonio Di Pietro, Luca Formaggia, and Roland Masson, editors, *Polyhedral Methods in Geosciences*, pages 119–158. Springer International Publishing, Cham, 2021. ISBN 978-3-030-69363-3. doi: [10.1007/978-3-030-69363-3\\_4](https://doi.org/10.1007/978-3-030-69363-3_4).
- [51] Volker Reichenberger, Hartmut Jakobs, Peter Bastian, and Rainer Helmig. A mixed-dimensional finite volume method for two-phase flow in fractured porous media. *Advances in water resources*, 29(7):1020–1036, 2006. doi: [10.1016/j.advwatres.2005.09.001](https://doi.org/10.1016/j.advwatres.2005.09.001).
- [52] Paola F Antonietti, Luca Formaggia, Anna Scotti, Marco Verani, and Nicola Verzott. Mimetic finite difference approximation of flows in fractured porous media. *ESAIM: Mathematical Modelling and Numerical Analysis*, 50(3):809–832, 2016. doi: [10.1051/m2an/2015087](https://doi.org/10.1051/m2an/2015087).
- [53] Luca Formaggia, Anna Scotti, and Federica Sottocasa. Analysis of a mimetic finite difference approximation of flows in fractured porous media. *ESAIM: Mathematical Modelling and Numerical Analysis*, 52(2):595–630, 2018. doi: [10.1051/m2an/2017028](https://doi.org/10.1051/m2an/2017028).
- [54] P. F. Antonietti, C. Facciola, A. Russo, and M. Verani. Discontinuous Galerkin approximation of flows in fractured porous media on polytopic grids. *SIAM J. Sci. Comput.*, 41(1):A109–A138, 2019. ISSN 1064-8275. doi: [10.1137/17M1138194](https://doi.org/10.1137/17M1138194).

- [55] Paola F Antonietti, Chiara Facciola, and Marco Verani. Polytopic discontinuous Galerkin methods for the numerical modelling of flow in porous media with networks of intersecting fractures. *Computers & Mathematics with Applications*, 116:116–139, 2022. doi: [10.1016/j.camwa.2021.08.015](https://doi.org/10.1016/j.camwa.2021.08.015).
- [56] Martin Vohralík. Equivalence between lowest-order mixed finite element and multi-point finite volume methods on simplicial meshes. *ESAIM: Mathematical Modelling and Numerical Analysis*, 40(2):367–391, 2006. doi: [10.1051/m2an:2006013](https://doi.org/10.1051/m2an:2006013).
- [57] Jhabriel Varela. `jhabriel/non_matching_estimates: mdnme v0.2`, December 2025.
- [58] Christophe Geuzaine and Jean-François Remacle. Gmsh: A 3-D finite element mesh generator with built-in pre-and post-processing facilities. *International journal for numerical methods in engineering*, 79(11):1309–1331, 2009. doi: [10.1002/nme.2579](https://doi.org/10.1002/nme.2579).